

1 **Title**

2 Rapid shelf-wide cooling response of a stratified coastal ocean to hurricanes

3

4 **Authors**

5 Greg Seroka<sup>1</sup>, Travis Miles<sup>1</sup>, Yi Xu<sup>2</sup>, Josh Kohut<sup>1</sup>, Oscar Schofield<sup>1</sup>, Scott Glenn<sup>1</sup>

6

7 <sup>1</sup>Center for Ocean Observing Leadership, Department of Marine and Coastal Sciences,

8 School of Environmental and Biological Sciences, Rutgers University, New Brunswick,

9 NJ 08901 USA

10 <sup>2</sup>State Key Laboratory of Estuarine and Coastal Research, East China Normal University,

11 3663 Zhongshan Road North, Shanghai 200062, China

12

13 Corresponding Author: Greg Seroka, Ocean Prediction Center, NOAA/NWS/NCEP,

14 5830 University Research Court, College Park, MD 20740 ([gregory.seroka@noaa.gov](mailto:gregory.seroka@noaa.gov))

15

16 **Key Points:**

17 1: Modeling is used to examine details of stratified coastal ocean cooling response to  
18 Hurricane Irene (2011), Tropical Storm Barry (2007)

19

20 2: Robust response: same baroclinic, mixing processes occurred in TCs on opposite ends  
21 of Mid-Atlantic track & seasonal stratification envelope

22

23 3: Coupled models predicting rapid ahead-of-eye-center TC cooling of a stratified  
24 coastal ocean critical for increasingly populated coastlines

25

26 **Index Terms:**

27 3372 Tropical cyclones, 4217 Coastal processes, 4255 Numerical modeling, 4572 Upper  
28 ocean and mixed layer processes, 4263 Ocean predictability and prediction

29 **Keywords:**

30 hurricanes, tropical cyclones, coastal oceanography, ocean modeling, gliders, continental  
31 shelf processes

32 **Abstract**

33           Large uncertainty in the predicted intensity of tropical cyclones (TCs) persists  
34 compared to the steadily improving skill in the predicted TC tracks. This intensity  
35 uncertainty has its most significant implications in the coastal zone, where TC impacts to  
36 populated shorelines are greatest. Recent studies have demonstrated that rapid ahead-of-  
37 eye-center cooling of a stratified coastal ocean can have a significant impact on hurricane  
38 intensity forecasts. Using observation-validated, high-resolution ocean modeling, the  
39 stratified coastal ocean cooling processes observed in two U.S. Mid-Atlantic hurricanes  
40 were investigated: Hurricane Irene (2011)—with an inshore Mid-Atlantic Bight (MAB)  
41 track during the late summer stratified coastal ocean season—and Tropical Storm Barry  
42 (2007)—with an offshore track during early summer. For both storms, the critical ahead-  
43 of-eye-center depth-averaged force balance across the entire MAB shelf included an  
44 onshore wind stress balanced by an offshore pressure gradient. This resulted in onshore  
45 surface currents opposing offshore bottom currents that enhanced surface to bottom  
46 current shear and turbulent mixing across the thermocline, resulting in the rapid cooling  
47 of the surface layer ahead-of-eye-center. Because the same baroclinic and mixing  
48 processes occurred for two storms on opposite ends of the track and seasonal  
49 stratification envelope, the response appears robust. It will be critical to forecast these  
50 processes and their implications for a wide range of future storms using realistic 3D  
51 coupled atmosphere-ocean models to lower the uncertainty in predictions of TC  
52 intensities and impacts and enable coastal populations to better respond to increasing  
53 rapid intensification threats in an era of rising sea levels.

54 **1. Introduction**

55           Although substantial progress in the prediction of tropical cyclone (TC) tracks has  
56 been realized globally over the past few decades, TC intensity prediction skill has  
57 remained comparatively flat across all TC ocean basins [*DeMaria et al.*, 2014; *Sopko and*  
58 *Falvey*, 2014; *Cangialosi and Franklin*, 2016]. This intensity gap can be traced to high  
59 resolution requirements for TC models, poor understanding and modeling of the  
60 atmospheric boundary layer, difficulty for many existing assimilation techniques to ingest  
61 observations of small but intense features, and—most importantly for this study—  
62 challenges in modeling the upper ocean response to TCs [*Emanuel*, 2016 and references  
63 within]. Large uncertainty in predicting the strength of TCs thus remains, which has its  
64 most significant implications for landfalling TCs where impacts to life and property—via  
65 storm surge, wind damage, and inland flooding—are greatest. These storms must first  
66 traverse the shallow, coastal ocean before making landfall. The number of studies in the  
67 literature investigating shallow, coastal ocean TC responses, indeed, pales in comparison  
68 to the number examining deep, open ocean TC responses [*Seroka et al.*, 2016]. Further,  
69 the differences between the deep, open ocean processes and the coastal processes are  
70 stark due to the influence of the bottom boundary layer and coastal wall in shallow water  
71 [*Glenn et al.*, 2016; *Seroka et al.*, 2016]. It is critical to close this gap, with the goal of  
72 improving the simulation of coastal ocean physics in coupled TC intensity models.

73           In the summer hurricane season, the shallow Mid Atlantic Bight (MAB) off the  
74 U.S. East Coast is one of the most seasonally-stratified regions in the world [*Schofield et*  
75 *al.*, 2008], characterized by a sun-heated warm (>25°C) and thin (10m or less) surface  
76 layer and a cold (<10°C) bottom layer termed the “Cold Pool” [*Houghton et al.*, 1982].

77 When Hurricane Irene traversed the highly stratified, shallow MAB waters in August  
78 2011 before making landfall in New Jersey, rapid surface cooling caused by mixing  
79 processes resulting from the two-layer baroclinic circulation in the MAB were observed  
80 by an underwater glider and several National Data Buoy Center (NDBC) buoys; these  
81 intense mixing processes and the surface cooling (up to 11°C) response in the MAB are  
82 described in detail in Glenn et al. [2016]. Because the magnitude of the cooling was so  
83 significant, it led to a reversal in the direction of air-sea latent and sensible heat fluxes—  
84 from the ocean providing heat to the storm when using a fixed pre-storm warm sea  
85 surface temperature (SST) bottom boundary condition to the ocean acting as a heat sink  
86 when using the fixed post-storm cold SST condition [Seroka et al., 2016].

87         This cooling was also found to primarily occur ahead of Irene’s eye center—  
88 critical for direct impact on storm intensity—as the storm traversed northeastward along  
89 the MAB coastline. The cascade of processes responsible were strong ahead-of-eye-  
90 center onshore winds and surface currents, coastal setup with water piling up along the  
91 coast, offshore bottom currents in response to the resulting offshore pressure gradient,  
92 and larger shear-driven turbulence, mixing, and entrainment of cold bottom water to the  
93 surface due to directly opposing onshore surface and offshore bottom currents.

94         The ahead-of-eye-center cooling signal that resulted from these baroclinic coastal  
95 ocean mixing processes was found to be present in the ten additional storms since 1985  
96 that traversed northeastward across the MAB in the summer stratified season, and also in  
97 Super Typhoon Muifa (2011) in the similarly highly-stratified Yellow Sea between  
98 eastern China and Korea. Further, this ahead-of-eye-center cooling was found to have a

99 large impact on Hurricane Irene’s intensity, larger than any other Weather Research and  
100 Forecasting (WRF) parameter tested [*Seroka et al.*, 2016].

101 Many questions remain. First, it is not known to what extent the ahead-of-eye-  
102 center cooling impacted the intensities of the other ten MAB storms and Typhoon Muifa.  
103 Extensive sensitivity studies like the one performed by Seroka et al. [2016] would need to  
104 be conducted for each storm to investigate these intensity impacts.

105 Second, it is not known if the same or different cooling processes occurred in the  
106 other ten MAB storms and in Typhoon Muifa. To improve understanding of TC coastal  
107 ocean response, the dominant momentum balances that occurred in these storms as well  
108 as mixing vs. advective processes that led to the ahead-of-eye-center cooling signals  
109 should be investigated in detail. It is also critical to understand the spatial—cross- and  
110 along-shelf, shallow and deep water—variability of the cooling processes, for a wider  
111 range of storms including Irene. Previous studies focused on these processes at the  
112 underwater glider location and not elsewhere on the MAB continental shelf [i.e. *Glenn et*  
113 *al.*, 2016]. These research gaps will guide this paper’s work.

114 Standard operational model annual performance metrics are based on the mean  
115 across all storms simulated during one or several hurricane seasons (e.g. [*Kim et al.*,  
116 2014; *Tallapragada et al.*, 2014; *Cangialosi and Franklin*, 2016]). While this method is  
117 effective in testing overall performance of a model, it tends to wash out any storm  
118 “personalities”—that is, unique characteristics—in both the atmosphere and the ocean.  
119 The full range of storm personalities represents the full range of storm air-sea feedbacks  
120 that coupled models should capture and resolve. Therefore, it is critical to not only  
121 improve models incrementally based on the mean in an operational environment (e.g.

122 [Kim *et al.*, 2014; Tallapragada *et al.*, 2014; Cangialosi and Franklin, 2016]), but also to  
123 investigate individual case studies and processes that models may or may not be correctly  
124 resolving (e.g. [D'Asaro *et al.*, 2007; Lin *et al.*, 2009; Jaimes and Shay, 2015; Glenn *et*  
125 *al.*, 2016; Seroka *et al.*, 2016]).

126         In order to better understand the baroclinic ocean response for different storms,  
127 further investigation was performed on Irene and Tropical Storm Barry (2007), one of the  
128 other ten MAB storms listed in Glenn *et al.* [2016]. For both of these storms, Rutgers  
129 University underwater gliders were deployed on the MAB continental shelf. Irene had a  
130 more inshore track northward through the MAB and Barry tracked farther offshore along  
131 the shelf break (Fig. 1). Irene occurred in late August toward the end of the MAB  
132 summer stratified season, while Barry occurred in early June, during the beginning of the  
133 summer stratified season. However, the intent is not to perform direct comparisons  
134 between the two storms, as this would introduce several uncontrollable variables and not  
135 be a fully controlled experiment. Rather, the objective is to better understand the  
136 conditions in both the atmosphere and ocean that may lead to the baroclinic coastal ocean  
137 cooling processes, ahead-of-eye-center cooling, and impact on storm intensities for two  
138 extremes in the storm track—one nearshore and one well offshore—and two extremes in  
139 summer stratification—one near the end and one near the beginning of the season. This  
140 paper will investigate the details of and variability in the dominant baroclinic coastal  
141 ocean processes—in both the cross- and along-shelf directions—for both Irene and Barry.  
142 By studying the spatiotemporal variability in these baroclinic coastal ocean cooling TC  
143 processes, the aim will be to improve the modeling of the full range of stratified coastal  
144 ocean TC responses.

145 **2. Data and Methods**

146 **2.1 High Frequency (HF) Radar**

147 Hourly surface ocean current data, one-hour center-averaged, from a network of  
148 CODAR Ocean Sensors SeaSonde HF Radar stations [Roarty *et al.*, 2010] along the  
149 MAB coast were used in this paper. Surface current map data have a nominal 6km spatial  
150 resolution (Fig 1).

151 **2.2 Gliders**

152 Teledyne-Webb Research (TWR) Slocum gliders, autonomous underwater  
153 vehicles (AUVs), were used in this paper [Schofield *et al.*, 2007; Glenn *et al.*, 2008,  
154 2016; Ruiz *et al.*, 2012; Miles *et al.*, 2013, 2015]. Rutgers University Gliders RU16  
155 (Irene) and RU17 (Barry) data were analyzed. Both gliders were equipped with a Seabird  
156 unpumped conductivity, temperature, and depth (CTD) sensor.

157 Depth- and time-averaged velocity calculations were performed using a dead-  
158 reckoning technique, a method typically used for underwater gliders [Sherman *et al.*,  
159 2001; Davis *et al.*, 2002; Schofield *et al.*, 2007]. To estimate bottom layer currents at the  
160 glider location, a combination of dead-reckoned depth-averaged glider currents and HF  
161 radar surface currents is used (Fig. 1). This method assumes that the HF radar surface  
162 currents are representative of the currents in the surface mixed layer above the  
163 thermocline. See [Glenn *et al.*, 2016] for detailed methods and equations used to calculate  
164 bottom layer currents.

165 **2.3 Bathymetry**

166 U.S. Coastal Relief Model data from the NOAA National Centers for  
167 Environmental Information were used for water depth and coastlines throughout this  
168 paper [*NOAA National Centers for Environmental Prediction, 2016*].

#### 169 **2.4 Satellite SST**

170 Advanced Very High Resolution Radiometer (AVHRR) data were used for ocean  
171 model SST verification. Techniques empirically-derived for the MAB to remove bright  
172 cloud covered pixels and retain darker ocean pixels were used to decloud AVHRR data  
173 but preserve the rapid TC cooling signal, following [*Glenn et al., 2016*].

#### 174 **2.5 Regional Ocean Modeling System (ROMS): ESPreSSO**

175 Ocean model simulations were conducted using ROMS [*Haidvogel et al., 2008*], a  
176 free-surface, sigma coordinate, primitive equation ocean model (code available at  
177 <http://www.myroms.org>). ROMS has been used for a wide variety of coastal applications.  
178 Specifically, the ESPreSSO (Experimental System for Predicting Shelf and Slope Optics)  
179 model [*Wilkin and Hunter, 2013*], covering the MAB from Cape Cod to south of Cape  
180 Hatteras, and from the inland bays to beyond the shelf break, was used for simulations.  
181 The ESPreSSO grid has a horizontal resolution of 5km and 36 vertical levels in a terrain-  
182 following s-coordinate system. The following were used in the ESPreSSO simulations:  
183 initial conditions developed from an ESPreSSO grid ROMS reanalysis with strong  
184 constrained four-dimensional variational (4D-Var) data assimilation, including  
185 assimilation of sea surface height, SST, HF radar surface currents, and in situ temperature  
186 and salinity observations; atmospheric forcing from North American Mesoscale (NAM)  
187 12km 3-hourly forecast data, using the COARE bulk formulae [*Fairall et al., 2003*] to  
188 calculate surface momentum and buoyancy fluxes; boundary conditions are daily two-

189 dimensional surface elevation and three-dimensional velocity, temperature, and salinity  
 190 fields from the Hybrid Coordinate Ocean Model (HYCOM) Navy Coupled Ocean Data  
 191 Assimilation (NCODA) forecast system; river inflows from the seven largest rivers, using  
 192 daily average U.S.G.S. discharge data; tidal boundary conditions from the ADvanced  
 193 CIRCulation (ADCIRC) tidal model; and vertical turbulence diffusivity using the general  
 194 length scale method k-kl type vertical mixing scheme [Umlauf and Burchard, 2003;  
 195 Warner *et al.*, 2005].

196 For Barry, the ROMS ESPreSSO simulation was initialized at 1200 UTC on May  
 197 29, 2007 and ended at 1200 UTC on June 8, 2007, with storm eye passage by glider  
 198 RU17 at 1700 UTC on June 4, 2007, just over five days into the simulation to allow for  
 199 model spin-up. For Irene, the ROMS ESPreSSO simulation was initialized at 1200 UTC  
 200 on August 24, 2011 and ended at 0000 UTC on September 3, 2011, with storm eye  
 201 passage by glider RU16 at 1200 UTC on August 28, 2011, exactly four days into the  
 202 simulation.

203 The depth-averaged momentum balance terms were direct output from the ROMS  
 204 simulations, and the equations are as follows:

$$\begin{aligned}
 \underbrace{\frac{\partial u}{\partial t}}_{\text{acceleration}} &= - \underbrace{\frac{\partial(uu)}{\partial x} - \frac{\partial(vu)}{\partial x}}_{\text{horizontal advection}} - \underbrace{\frac{1}{\rho_0} \frac{\partial P}{\partial x}}_{\text{pressure gradient}} + \left( \underbrace{\frac{\tau_s^x}{h\rho_0}}_{\text{surface stress}} - \underbrace{\frac{\tau_b^x}{h\rho_0}}_{\text{bottom stress}} \right) + \underbrace{fv}_{\text{Coriolis}}
 \end{aligned}
 \tag{1}$$

205  
206

$$\begin{aligned}
 \underbrace{\frac{\partial v}{\partial t}}_{\text{acceleration}} &= - \underbrace{\frac{\partial(uv)}{\partial x} - \frac{\partial(vv)}{\partial x}}_{\text{horizontal advection}} - \underbrace{\frac{1}{\rho_0} \frac{\partial P}{\partial y}}_{\text{pressure gradient}} + \left( \underbrace{\frac{\tau_s^y}{h\rho_0}}_{\text{surface stress}} - \underbrace{\frac{\tau_b^y}{h\rho_0}}_{\text{bottom stress}} \right) - \underbrace{fu}_{\text{Coriolis}}
 \end{aligned}
 \tag{2}$$

207  
208

209

210 where  $u$  and  $v$  are the along-shelf and cross-shelf components of depth-averaged velocity  
 211 respectively,  $t$  is time,  $P$  is depth-averaged pressure,  $\rho_o$  is a reference density,  $\tau_s$  and  $\tau_b$  are  
 212 surface (wind) and bottom stresses,  $h$  is water column depth, and  $f$  is the latitude-  
 213 dependent Coriolis frequency. Horizontal diffusion was small and neglected here.

214 The temperature rate equation terms to diagnose advection vs. mixing were also  
 215 direct output from ROMS. The equation is as follows:

$$\frac{\partial T}{\partial t} = -\frac{\partial(uT)}{\partial x} - \frac{\partial(vT)}{\partial y} - \frac{\partial(wT)}{\partial z} + \frac{\partial A_{kt}}{\partial z} \frac{\partial T}{\partial z} + D_T + F_T$$

216 (3)

217 with the following surface and bottom boundary conditions, respectively:

$$\left( A_{kt} \frac{\partial T}{\partial z} \right)_{z=0} = \frac{Q_{net}}{\rho_o C_p}$$

218 (4)

$$\left( A_{kt} \frac{\partial T}{\partial z} \right)_{z=h} = 0$$

219 (5)

220 Here,  $T$  is the temperature,  $t$  is time,  $u$ ,  $v$ , and  $w$  are the along-shelf, cross-shelf and  
 221 vertical components of velocity.  $A_{kt}$  is the vertical diffusivity coefficient,  $D_T$  is the  
 222 horizontal diffusion term and  $F_T$  is friction.  $Q_{net}$  is the surface net heat flux,  $\rho_o=1025$ ,  
 223  $\text{kg m}^{-3}$  is a reference density,  $C_p=3985 \text{ J (kg } ^\circ\text{C)}^{-1}$  is the specific heat capacity of  
 224 seawater and  $h$  is the water depth. Horizontal diffusion again was small and neglected  
 225 here.

## 226 3. Results

### 227 3.1 Observations

228 Glenn et al. [2016] used HF radar and glider RU16 data to determine surface,  
 229 depth-averaged, and bottom currents at the glider location during Irene. Part of the time

230 series is repeated here in Fig. 1 for ease of comparison to a similar analysis for Barry. At  
231 0600 UTC on August 28, 2011, less than four hours before Irene's NJ landfall and eye  
232 passage by glider RU16, surface ocean currents were directed onshore and upshelf,  
233 aligning close to the onshore winds ahead of Irene's eye (Fig. 1, top left). Current  
234 magnitudes at this time approached  $1 \text{ m s}^{-1}$ . At 0200 UTC on June 4, 2007, a full 15  
235 hours before Barry's eye passage by glider RU17, surface ocean currents were in a very  
236 similar direction, onshore and upshelf.

237 Time series of temperature profiles at the glider locations below the surface  
238 current maps indicate initially very strong stratification and an eventual breakdown in  
239 stratification upon storm forcing. For Irene in late August, surface mixed layer  
240 temperatures approached  $25^{\circ}\text{C}$  to  $\sim 10\text{-}15\text{m}$  depth, and bottom MAB Cold Pool  
241 temperatures were less than  $10^{\circ}\text{C}$ . For Barry in early June, surface mixed layer  
242 temperatures down to  $\sim 10\text{-}15\text{m}$  depth were approaching  $16^{\circ}\text{C}$  with bottom MAB Cold  
243 Pool temperatures again less than  $10^{\circ}\text{C}$ , approaching  $5^{\circ}\text{C}$ . For Irene, the thermocline  
244 (black contour) deepened to  $\sim 30\text{m}$  depth and surface mixed layer temperatures cooled to  
245  $\sim 17^{\circ}\text{C}$ , with much ( $\sim 5^{\circ}\text{C}$ , or  $\sim 75\%$ ) of the cooling occurring ahead-of-eye-center. For  
246 Barry, the thermocline (black contour) deepened briefly to  $25\text{m}$  depth and surface mixed  
247 layer temperatures cooled to nearly  $14^{\circ}\text{C}$ , with 100% of the cooling at RU17 occurring  
248 ahead-of-eye-center.

249 Cross-shelf and along-shelf surface (red), depth-averaged (green), and bottom  
250 (blue) current time series are depicted in the two panels below the temperature time series  
251 in Fig. 1. For Irene, currents in Earth coordinates are rotated  $31^{\circ}$  clockwise from north to  
252 attain cross- and along-shelf components. For Barry, currents in Earth coordinates are

253 rotated 50° clockwise from north to attain cross- and along-shelf components. For both  
254 Irene and Barry, red surface currents peaked onshore ahead-of-eye-center, and blue  
255 bottom currents peaked offshore at the same time yet with a bit of a lag in set up. For  
256 Irene, along-shelf currents were very small ahead-of-eye-center, but for Barry, along-  
257 shelf surface currents to the northeast peaked ahead-of-eye-center and bottom currents  
258 peaked just before. For both storms, observations indicate a two-layer circulation, with  
259 cross-shelf surface currents onshore and cross-shelf bottom currents offshore, enhancing  
260 the shear and resultant mixing and cooling. For Barry, a similar surface to bottom shear  
261 profile occurred in the along-shelf direction. The bottom right panel in Fig. 1 shows a  
262 calculation of surface to bottom shear, combining both the along- and cross-shelf  
263 components for Barry due to the large observed along-shelf component. Maximum shear  
264 occurred at the same time as maximum surface cooling and thermocline deepening, and  
265 well before eye passage.

## 266 **3.2 Modeling**

267 In order to investigate the details of the baroclinic processes and mixing that  
268 occurred in Irene and Barry, including momentum balance analysis and the temperature  
269 diagnostic equation for mixing vs. advection comparisons, ROMS ESPreSSO simulations  
270 were performed as described in Section 2.5 above.

### 271 **3.2.1 ROMS Simulation Validation: Hurricane Irene (2011)**

272 A pre-storm map of SST over the MAB from AVHRR at 0742 UTC on August  
273 24, 2011 (Fig. 2, top left) shows coastal upwelling along the NJ, DE, and MD coastlines,  
274 with a warm tongue of SST through the southern MAB and extending offshore of the  
275 50m isobath and into the northern MAB north of the Hudson Canyon. The ROMS

276 ESPreSSO re-run SST ~four hours later (Fig. 2, top right) shows very good agreement  
277 with AVHRR, capturing the coastal upwelling, warm tongue, Gulf Stream, and colder  
278 waters south of Rhode Island and Nantucket.

279 A post-storm map of SST over the MAB from AVHRR at 0828 UTC on August  
280 29, 2011 (Fig. 2, middle left) shows a much different story, with cold  $<18^{\circ}\text{C}$  SST from  
281 the mouth of the Hudson Canyon and northward, and a corridor of colder water at the  
282 50m isobath and offshore in the southern MAB. The ROMS ESPreSSO re-run SST (Fig.  
283 2, middle right) again shows very good agreement with AVHRR, with perhaps the only  
284 minor issue being not as cold water at the mouth of the Delaware Bay and in the southern  
285 MAB.

286 A difference map of post-storm minus pre-storm AVHRR SST (Fig. 2, bottom  
287 left) shows maximum cooling (approaching  $11^{\circ}\text{C}$ ) at the mouth of the Hudson Canyon  
288 and across the MAB, with less cooling in the shallow regions of the shelf and offshore in  
289 the deep water. Again, ROMS (Fig. 2, bottom right) agrees very well with the AVHRR  
290 cooling map, capturing the maximum in cooling at the Hudson Canyon mouth.

291 Finally, RU16 glider temperature profile time series (Fig. 3, left) shows the same  
292 deepening of the thermocline and cooling of the surface layer as shown in Fig. 1. ROMS  
293 (Fig. 3, right) taken at the closest grid cell to the average position of RU16 during the  
294 storm period shows an initial thermocline ~10-15m too deep but with correct surface  
295 mixed layer and bottom layer temperatures. Although the simulated thermocline is deeper  
296 than observed, the two-layer structure is present to support the relevant processes. Upon  
297 storm forcing, the ROMS thermocline deepens to the correct depth, but the surface does  
298 not sufficiently cool, likely due to the inadequate supply of cold bottom water at the start.

299 Despite deficiencies in the details, the overall storm response characteristics—two-layer  
300 structure at the start, deepening of the thermocline, and rapid and intense cooling of the  
301 surface mixed layer—are present and adequate for determining dominant force balances  
302 and diagnosing the causes of SST cooling.

### 303 **3.2.2 ROMS Simulation Validation: Tropical Storm Barry (2007)**

304 A pre-storm map of SST over the MAB from AVHRR at 0559 UTC on June 2,  
305 2007 (Fig. 4, top left) is partially blocked by clouds but shows a warm Gulf Stream  
306 offshore, a couple Gulf Stream rings to the northwest in the slope water, a ribbon of  
307 colder water along the shelf break at 200m, a ribbon of warmer water inshore of the 50m  
308 isobath, and coastal upwelling east of Cape May, NJ, at the mouth of Delaware Bay, and  
309 along the Delmarva Peninsula. ROMS (Fig. 4, top right) shows good agreement with  
310 AVHRR, with a warm Gulf Stream, cold water to the north, NJ and Delaware Bay coastal  
311 upwelling, warmer mid-shelf MAB waters, and a hint of the warm Gulf Stream filament  
312 approaching the 200m isobath.

313 A post-storm map of SST over the MAB from AVHRR at 0207 UTC on June 5,  
314 2007 (Fig. 4, middle left) with the same color bar as the top panels in Fig. 4 shows cooler  
315 water over the northern MAB, and ROMS at the same time (Fig. 4, middle right)  
316 provides a similar picture. The difference maps of post-storm minus pre-storm AVHRR  
317 SST (Fig. 4, bottom left), ROMS re-run at the same time difference (Fig. 4, bottom  
318 middle), and ROMS re-run to maximize cooling (Fig. 4, bottom right) highlight the  
319 cooling and warming patterns across the MAB. Although clouds block parts of the map,  
320 AVHRR shows a pattern of warming in the southern MAB and offshore, and cooling in  
321 the northern MAB and offshore. Both ROMS re-run difference maps show more

322 widespread cooling, with slight warming offshore NJ and off the Delmarva Peninsula,  
323 and where the Gulf Stream meanders moved through time.

324 Finally, the profile time series of temperature at the RU17 glider location (Fig. 5,  
325 left) again shows surface mixed layer cooling and deepening during the storm period, as  
326 in Fig. 1. ROMS ESPreSSO re-run (Fig. 5, right) shows a thermocline initially 15-20m  
327 too deep, but surface and bottom temperatures overall correct. The resulting cooling of  
328 the surface layer occurs at about the correct time, but the surface layer warming post-  
329 storm does not occur.

### 330 **3.2.3 Temperature, current, shear, and momentum balance spatial time series: Irene**

331 At the cross section location near RU16 noted by the northwest to southeast black  
332 dots in Fig. 2, Hövmoller diagrams of time (increasing up) vs. distance offshore were  
333 produced. Surface temperature (Fig. 6, top left) shows initially warm surface water  
334 stretching from the edge of the coastal upwelling to >200km offshore. Then, SST rapidly  
335 cools across the shelf and in deep water, so that any cooling after eye passage (from  
336 NAM—two hours later than observed) is minimal. No SST cooling occurred within the  
337 nearshore coastal upwelling region. Bottom temperature (Fig. 6, bottom left) shows a  
338 warm downwelling bulge during the storm, starting at the coastline and extending to  
339 close to 50km offshore. The core of the MAB Cold Pool can be seen around 100km  
340 offshore. Four sample locations are noted with the vertical solid lines labeled 1) in the  
341 upwelling region, 2) near RU16, 3) in the core of the Cold Pool, and 4) in deep water.  
342 These four locations will be used in the temperature diagnostic analysis, Section 3.2.5.

343 A Hövmoller of cross-shelf surface currents (Fig. 6, top middle) show onshore  
344 currents increasing at about 0000 UTC on August 28, from about 50km offshore across

345 the shelf and into some of the deeper water. For Irene model results, currents in Earth  
346 coordinates are again rotated  $31^\circ$  clockwise from north to attain cross- and along-shelf  
347 components. The onshore surface currents peak at around 0300 UTC, and then decrease a  
348 few hours before eye passage. Bottom currents (Fig. 6, bottom middle) are opposing  
349 offshore across the shelf and weaker than the onshore surface currents. The bottom  
350 onshore currents begin again at about 0000 UTC on August 28, and last until eye  
351 passage. After eye passage, surface currents switch to offshore, with the switch nearshore  
352 occurring a few hours after eye passage likely due to tidal influence (not shown). Bottom  
353 currents switch to onshore after eye passage almost immediately. Maximum shear from  
354 this plot occurred roughly from 0000 to 1200 UTC on August 28, and reversed from 1500  
355 UTC on August 28 to 0000 UTC on August 29.

356         The along-shelf surface current Hövmoller (Fig. 6, top right) shows northeastward  
357 currents ahead of and after eye passage, with southwestward surface currents after eye  
358 passage in deeper water. Bottom currents (Fig. 6, bottom right) are southwestward ahead  
359 of eye passage and immediately after, then northeastward later at 0000 UTC on August  
360 29. Maximum shear from this plot occurred roughly from 0600 to 1500 UTC on August  
361 28.

362         A bulk surface to bottom shear Hövmoller diagram, comprised of the cross- and  
363 along-shelf components, is shown in Fig. 7 (left panel). This bulk shear Hövmoller shows  
364 a symmetric  $\sim 50\%$  ahead and  $50\%$  behind eye shear pattern in deep water, consistent  
365 with Price [1981]. In the shallow water over the continental shelf, shear is skewed ahead-  
366 of-eye-center. Because in deep water the bottom layer is quiescent and in shallow water  
367 the bottom layer is moving, only qualitative comparisons between deep and shallow

368 water can be made. Additionally, bottom currents in shallow water are affected by  
369 opposing bottom stress, restricting any quantitative comparisons between deep and  
370 shallow water. By changing bottom currents to 0, a more evenly distributed shear pattern  
371 between ahead of and behind eye passage results (Fig. 7, right), showing that the  
372 opposing bottom currents in the two-layer circulation has an influence on the shear  
373 pattern.

374         The ahead-of-eye-center cooling due to this shear is greater than behind-eye  
375 cooling (Fig. 6, top left), potentially because 1) behind the eye center the water column is  
376 already mixed, and the surface layer is already deeper, 2) there are weaker backside  
377 offshore winds than front-side onshore winds due to frictional land effects, and 3) the  
378 front side of Irene cools the SST, the eye moves over the cooler water and weakens the  
379 storm, and the backside is weaker. As will be shown in the following momentum balance  
380 Hövmollers, the dominant cross-shelf momentum terms are onshore wind stress balanced  
381 by offshore pressure gradient force ahead-of-eye-center, and offshore wind stress  
382 balanced by onshore pressure gradient force behind-eye-center. This balance is likely due  
383 to the presence of the coastline and shallow bottom, in which onshore surface winds  
384 ahead-of-eye-center pile water at the coast and result in the offshore bottom current, and  
385 offshore surface winds behind-eye-center push water away from the coast and result in  
386 the onshore bottom current. In both cases—ahead-of-eye-center and behind-eye-center—  
387 a two-layer circulation occurs due to the presence of the coastline, shallow bottom, and  
388 stratified water column.

389         The depth-averaged cross-shelf momentum balance time series (Fig. 8) depicts all  
390 terms except for horizontal viscosity, which was very small. Acceleration shows a

391 strongly tidal signal, with less onshore acceleration just before eye passage. Wind stress  
392 is strongly onshore ahead-of-eye passage, and switches to offshore after. Pressure  
393 gradient force is offshore ahead-of-eye-center from the coast all the way to the shelf  
394 break, and then switches to offshore mid-shelf first and then both nearshore and near the  
395 shelf break second; this pressure gradient pattern is due to coastal set up ahead-of-eye and  
396 coastal set down behind-eye. Coriolis is offshore, increasing after the eye. Bottom stress  
397 is onshore opposing the offshore bottom currents ahead-of-eye, and then switches sign  
398 after eye. Finally, advection is small and noisy, with a response near the inertial period  
399 especially near the shelf break. The dominant cross-shelf force balance progresses from –  
400 wind stress balanced by +pressure gradient ahead-of-eye-center, to +wind stress  
401 +Coriolis balanced by –pressure gradient after eye passage until 0000 UTC on August  
402 29, and finally to a geostrophic balance of +Coriolis balanced by –pressure gradient.

403 In the along-shelf direction, depth-averaged momentum balance terms (Fig. 9) are  
404 generally smaller than the cross-shelf terms. Again, acceleration has a tidal signal, but so  
405 does Coriolis. The dominant along-shelf force balance progresses from –wind stress  
406 balanced by +pressure gradient and +Coriolis, to +wind stress balanced by –pressure  
407 gradient and –Coriolis, and finally to +/- pressure gradient balanced by +/- Coriolis (tidal  
408 periodicity).

#### 409 **3.2.4 Temperature, current, shear, and momentum balance spatial time series:**

##### 410 **Barry**

411 The time series of SST for Barry (Fig. 10, top left) was taken at the northern  
412 WNW to ESE cross section location just north of the Hudson Canyon as indicated by the  
413 black dots in Fig. 4. This northern location was chosen to target the greatest SST cooling

414 in Barry. A similar cooling signal is apparent across the shelf and even in deep water. At  
415 National Data Buoy Center (NDBC) station ALSN6, the Barry station used by [*Glenn et*  
416 *al.*, 2016] for the ahead-of-eye-center cooling signal, cooling ( $\sim 3.5^{\circ}\text{C}$ ) was greatest. At  
417 the warm strip of water indicated by the vertical line labeled “2”, and in the deep water,  
418 total cooling was less than  $1^{\circ}\text{C}$ . The bottom temperature spatial time series (Fig. 10,  
419 bottom left) shows a similar but more subtle downwelling bulge from the coast as was  
420 evident in Irene. Five sample locations are noted with the vertical solid lines labeled 1) in  
421 the nearshore maximum cooling and near ALSN6, 2) in the warm strip of water, 3) in the  
422 core of the Cold Pool, 4) near RU17, and 5) in deep water. These five locations will be  
423 used in the temperature diagnostic analysis, Section 3.2.6.

424 The cross-shelf surface current time series (Fig. 10, top middle) shows onshore  
425 surface currents peaking 12-18 hours prior to eye passage, but remaining weakly onshore  
426 until eye passage. For Barry model results, currents in Earth coordinates are again rotated  
427  $51^{\circ}$  clockwise from north to attain cross- and along-shelf components. Bottom currents  
428 (Fig. 10, bottom middle) show a primarily tidal signal, with alternative offshore and  
429 onshore bottom currents. Maximum shear was roughly 0600 to 1200 UTC on June 4.  
430 This maximum shear occurs when the bottom offshore currents (mainly tidal) oppose the  
431 onshore surface currents. Because the storm forcing is weaker than in Irene, the tidal  
432 signal dominates the bottom current forcing. This is consistent with the findings of Keen  
433 and Glenn [1995], who found that during a storm crossing the MAB in October 1990, the  
434 tidal signal dominated the bottom current forcing, and storm sedimentation was directly  
435 related to the tidal flow.

436           In the along-shelf direction, surface currents were northeastward before eye  
437 passage and southwestward after (Fig. 10, top right). Bottom currents were  
438 southwestward the entire storm period, both before and after eye passage. A similar  
439 analysis just south of the Hudson Canyon may help answer why this occurred. One  
440 potential reason is that the Hudson Canyon acted as a barrier, blocking bottom currents  
441 from crossing the large bathymetric gradients.

442           The bulk surface to bottom shear Hövmoller for Barry, comprised of the cross-  
443 and along-shelf shears, is shown in Fig. 11 (left panel). This bulk shear Hövmoller again  
444 shows a roughly symmetric ~50% ahead and 50% behind eye shear pattern in deep water  
445 if the time period of 0000 UTC on June 4 to 0600 UTC on June 5 is used. Again, like for  
446 Irene, shear is skewed ahead-of-eye passage in the shallow water, and by substituting 0  
447 for bottom currents, a more (but not quite fully) symmetric shear pattern in shallow water  
448 results (Fig. 11, right).

449           The Hövmoller cross-shelf depth-averaged momentum balance terms (Fig. 12)  
450 show a strongly tidal signal in the acceleration, pressure gradient, and Coriolis terms  
451 across the shelf, and in the bottom stress and horizontal advection terms very near shore.  
452 Wind stress was directed onshore ahead of eye passage and weakly offshore after.  
453 Pressure gradient was primarily tidal, with more positive offshore values along the shelf  
454 break just ahead of eye passage as compared to after eye passage. Coriolis was largely  
455 tidal and onshore, with the maximum again at the shelf break. Bottom stress was mostly  
456 tidal, but mostly negative opposing the offshore bottom currents at about 0600 UTC on  
457 June 4 ahead of eye, when the downwelling circulation aligned with the tidal signal.  
458 Finally, horizontal advection was mostly small. The dominant depth-averaged cross-shelf

459 force balance progressed from  $-$ wind stress balanced by  $+$ pressure gradient ahead of eye  
460 passage, to  $+$ wind stress balanced by  $+/-$ Coriolis and  $+/-$  pressure gradient (tidal  
461 periodicity) just after eye passage, to quasi-geostrophic balance with  $+/-$ Coriolis  
462 balanced by  $+/-$  pressure gradient (again tidal).

463 The Hövmoller along-shelf depth-averaged momentum balance terms (Fig. 13)  
464 show a mostly tidally-forced signature. Acceleration was mostly tidal, with slightly more  
465 negative onshore (or less positive offshore) acceleration ahead of eye passage from 0000  
466 to  $\sim$ 0900 UTC on June 4. Wind stress was southwestward ahead of eye passage and  
467 northeastward after. Pressure gradient and Coriolis terms were primarily tidal, bottom  
468 stress was always northeastward opposing the southwestward bottom currents, and  
469 horizontal advection was small. The dominant along-shelf depth-averaged momentum  
470 balance progressed from  $-$ wind stress balanced by  $+$ bottom stress and a residual in the  
471 alternating  $+/-$  pressure gradient term and  $+/-$  Coriolis term ahead of eye passage, to  
472  $+$ wind stress balanced by  $+/-$ Coriolis and  $+/-$ pressure gradient behind eye passage.

473 The shelf break maxima in the pressure gradient and Coriolis terms could be due  
474 to the presence of a warm core ring starting pre-storm just north of the Hudson Canyon  
475 and the northern cross section location (Fig. 4, top left) and moving southeastward by  
476 post-storm (Fig. 4, middle left). This ring, moving along the shelf break and beginning to  
477 impinge onto the shelf, forces a geostrophic circulation at the shelf break front [*Zhang*  
478 *and Gawarkiewicz, 2015*], which is evident at the shelf break in both the cross- and  
479 along-shelf momentum balance Hövmollers (Figs. 12 and 13).

### 480 **3.2.5 Advection vs. Mixing Temperature Response: Irene**

481           The temperature diagnostic equation terms were plotted for Irene (Fig. 14) at the  
482 points indicated by the large red dots on Fig. 2 and by the vertical solid black lines on the  
483 left panels of Fig. 6 to determine the primary cause of cooling. The left panel is within  
484 the upwelling region, the second is at RU16, the third is in the MAB Cold Pool core, and  
485 the fourth is in deep water. At the top is the full temperature rate term, in the middle is  
486 the vertical diffusion term, and at the bottom are the vertical plus horizontal advection  
487 terms. Horizontal diffusion was not plotted, as it was very small. First, a general tidal  
488 signal is apparent in the full temperature rate term, primarily due to advection at all four  
489 locations. Cooling in the mixed layer was due to vertical diffusion at all four points, with  
490 ahead-of-eye-center cooling occurring at points #1, 2, and 3. At point 1 within the  
491 upwelling, surface mixed layer cooling stopped once the thermocline reached the bottom  
492 of the water column, as the source of cold water was removed (Fig. 14 left middle). At  
493 point 2 near RU16, ahead-of-eye-center cooling was caused by vertical diffusion cooling  
494 being skewed ahead-of-eye-center. At point 3 in the Cold Pool core, vertical diffusion  
495 cooling was also skewed ahead-of-eye-center, with advection warming after eye passage.  
496 Finally, at point 4 in the deep water, a deep, cold quiescent bottom allowed for some cold  
497 water to entrain into the thick ~200m surface mixed layer ahead-of-eye passage, with an  
498 advective signal dominating after eye passage.

### 499 **3.2.6 Advection vs. Mixing Temperature Response: Barry**

500           The temperature diagnostic equation terms plotted for Irene at four locations in  
501 Fig. 14 were also plotted for Barry at five locations in Fig. 15. These five locations are  
502 indicated by the large red dots in Fig. 4 and the vertical solid black lines in the left panels  
503 of Fig. 10. For Barry, the left panel of Fig. 15 is near ALSN6, the second panel is within

504 the warm strip of water, the third panel is within the Cold Pool core, the fourth is near  
505 RU17, and the fifth is in deep water. Again, a tidal advection signal is apparent, with  
506 vertical diffusion not exhibiting any tidal cooling/warming signal. Vertical diffusion  
507 again caused cooling in the mixed layer except at point 5 in the deep water. Point 5 looks  
508 primarily advective with a deep quiescent bottom. At points 1-4 the tidal advection  
509 cooling/warming periodicity was modulated by the vertical diffusion cooling, which  
510 looks to be skewed ahead-of-eye passage during the greatest shear period (Fig. 11 left).

#### 511 **4. Summary**

512 Baroclinic coastal ocean cooling processes were investigated in detail for  
513 Hurricane Irene (2011) and Tropical Storm Barry (2007), two summer TCs, both with  
514 rapid ahead-of-eye-center cooling, but with different tracks and occurring at different  
515 times in the summer season. Cross-shelf variability in the depth-averaged momentum  
516 balance terms demonstrated that the dominant force balance driving the baroclinic  
517 circulation was the same across the entire MAB shelf. Cross-shelf variability in the  
518 temperature diagnostic equations showed that the resultant ahead-of-eye-center cooling  
519 of the surface layer in both storms was dominated by mixing rather than advection.

520 For Irene, it was previously found that cross-shelf two-layer surface to bottom  
521 opposing current shear was large and along-shelf surface to bottom shear was small at the  
522 RU16 glider location [*Glenn et al.*, 2016]. Here, for Barry, it was found that both the  
523 cross- and along-shelf components of the surface to bottom opposing current shear  
524 contributed to the mixing and cooling observed at the RU17 glider location. For both  
525 storms, analysis of bulk shear (including both cross- and along-shelf shear components)  
526 indicated a symmetric 50% ahead and 50% behind eye shear pattern in deep water, but

527 with maximum shear skewed ahead-of-eye-center in the shallow water over the  
528 continental shelf. This ahead-of-eye-center skewing of the vertical shear was found to  
529 occur not only due to opposing bottom currents over the shelf before the eye, but also due  
530 to weaker winds and a deeper surface layer after the eye.

531 For Irene, the dominant force balance ahead of eye passage was onshore wind  
532 stress balanced by offshore pressure gradient, and the large offshore pressure gradient  
533 term stretched across the entire shelf. The wind stress and pressure gradient terms  
534 switched directions right after eye passage and eventually the force balance evolved to  
535 geostrophic long after the storm. For Barry, the dominant force balance on the shelf  
536 ahead of eye passage was modulated by the tides but also had the onshore wind stress  
537 term balanced by offshore pressure gradient, and again the large offshore pressure  
538 gradient term extended all the way across the shelf. The along-shelf force balance also  
539 played a role for Barry, potentially due to the location of the cross section relative to the  
540 changing slopes of the bathymetry just north of the Hudson Canyon. In both the cross-  
541 and along-shelf directions, independent of the wind forcing, there was a maximum in the  
542 pressure gradient and Coriolis terms near the shelf break, which coincided with a warm  
543 eddy moving southwestward along the shelf slope front with a geostrophic circulation.

544 Finally, cross-shelf variability in the temperature change diagnostic terms was  
545 investigated. For both storms in the shallow water on the shelf, vertical diffusion was the  
546 main cause of the mostly ahead-of-eye-center cooling in the surface mixed layer. Tidal  
547 periodicity of cooling/warming was apparent in the combined vertical and horizontal  
548 advection terms. Cooling in the surface layer due to vertical diffusion did occur within  
549 the coastal upwelling during Irene, and the cooling stopped once the thermocline hit the

550 bottom of the water column as the bottom cold water was also removed. In deep water,  
551 vertical diffusion and advection were important drivers of mixed layer cooling for Irene,  
552 whereas for Barry in deep water, advection was the main driver in the periodic and  
553 alternating warming/cooling near the surface.

554         The drivers for the major differences in coastal ocean response between Irene and  
555 Barry were storm track, structure, intensity, and time of year. Irene had a more inshore  
556 MAB track during the late summer stratified season, whereas Barry was weaker with a  
557 farther offshore track during the early summer stratified season. Due to the offshore  
558 track, MAB surface winds for Barry had a more along-shelf component than the  
559 primarily cross-shelf winds during Irene, leading to both cross- and along-shelf  
560 components playing a larger role in the coastal ocean response for Barry, and a primarily  
561 cross-shelf response for Irene.

## 562 **5. Discussion**

563         Glenn et al. [2016] identified 11 summer storms that traversed northeastward  
564 across the MAB and that exhibited a range of ahead-of-eye-center cooling. Here, we  
565 selected two extreme cases—both with an underwater glider deployed—from this  
566 envelope: one with an offshore track and the other with an inshore one. One was near the  
567 beginning of the summer stratified season and the other near the end. Indeed, differences  
568 in the details exist between the two storm extremes—from the along-shore component  
569 playing a larger role in Barry’s force balance, to the alternating warming/cooling  
570 advective tidal signal playing a larger role in Barry’s temperature response. Nevertheless,  
571 both storms exhibited a two-layer baroclinic circulation, forced by an offshore pressure  
572 gradient opposing the onshore wind stress ahead-of-eye-center and extending across the

573 entire MAB shelf. Cooling in both storms was mostly ahead-of-eye-center and dominated  
574 by vertical shear-induced mixing. These commonalities across the two storm extremes  
575 indicate that the process is robust and can be expected on stratified continental shelves  
576 over a wide range of TC scenarios.

577         Because this process is robust across these two extreme cases drawn from the 30-  
578 year envelope of MAB summer cyclones, it will be critical to resolve and forecast the  
579 same process for future storms, with the goal of lowering the uncertainty in predictions of  
580 TC impacts. Realistic 3D coupled models that assimilate coastal observatory data and  
581 that are capable of predicting the ahead-of-eye-center stratified coastal ocean cooling  
582 processes will be critical. The increasingly populated [*Peduzzi et al.*, 2012] at-risk  
583 coastlines—the Northeast U.S. and northeastern China and Korea—adjacent to the two  
584 most stratified seas in the world—the MAB and Yellow Sea—will be increasingly  
585 vulnerable to TCs as sea levels rise [*Hansen et al.*, 2016], as TCs more frequently and  
586 severely undergo rapid intensification just before landfall [*Emanuel*, 2016], and if  
587 maximum TC intensities continue to migrate poleward [*Kossin et al.*, 2014]. By lowering  
588 uncertainty in coastal TC intensity forecasts through models that resolve these stratified  
589 coastal ocean cooling processes, these populations can better prepare for and respond to  
590 these rising threats.

591

## 592 **Acknowledgments**

593 Support was provided by New Jersey Board of Public Utilities (2010RU-COOL, BP-  
594 070), the Environmental Protection Agency (EP-11-C-000085), New Jersey Department  
595 of Environmental Protection (WM13-019-2013), National Oceanic and Atmospheric

596 Administration (NOAA) led Integrated Ocean Observing System through the Mid-  
597 Atlantic Regional Association Coastal Ocean Observing System (MARACOOS,  
598 NA11NOS0120038), NOAA Cooperative Institute for the North Atlantic Region  
599 (NA13OAR4830233), and Rutgers University. We would like to thank John Wilkin and  
600 Julia Levin at Rutgers University for their suggestions regarding the ocean modeling, the  
601 Rutgers Ocean Modeling research associates for their ROMS help, and Rich Dunk for his  
602 helpful meteorological discussions and ideas. Model output and observations are  
603 available upon request.

604  
605

606 **References**

- 607 Cangialosi, J. P., and J. L. Franklin (2016), *National Hurricane Center Forecast*  
 608 *Verification Report: 2015 Hurricane Season*.
- 609 D’Asaro, E., T. B. Sanford, P. P. Niiler, and E. J. Terrill (2007), Cold wake of Hurricane  
 610 Frances, *Geophys. Res. Lett.*, *34*(15), 2–7, doi:10.1029/2007GL030160.
- 611 Davis, R. E., C. C. Eriksen, and C. P. Jones (2002), Autonomous Buoyancy-driven  
 612 Underwater Gliders, *Technol. Appl. Auton. Underw. Veh.*, 37–58.
- 613 DeMaria, M., C. R. Sampson, J. A. Knaff, and K. D. Musgrave (2014), Is tropical  
 614 cyclone intensity guidance improving?, *Bull. Am. Meteorol. Soc.*, *95*(3), 387–398,  
 615 doi:10.1175/BAMS-D-12-00240.1.
- 616 Emanuel, K. (2016), Will Global Warming Make Hurricane Forecasting More Difficult?,  
 617 *Bull. Am. Meteorol. Soc.*, doi:10.1175/BAMS-D-16-0134.1, in press.
- 618 Fairall, C. W., E. F. Bradley, J. E. Hare, and A. A. Grachev (2003), Bulk  
 619 parameterization of air-sea fluxes: Updates and verification for the COARE  
 620 algorithm, *J. Clim.*, *16*(4), 571–591.
- 621 Glenn, S., C. Jones, M. Twardowski, L. Bowers, J. Kerfoot, J. Kohut, D. Webb, and O.  
 622 Schofield (2008), Glider observations of sediment resuspension in a Middle Atlantic  
 623 Bight fall transition storm, *Limnol. Oceanogr.*, *53*(5 part 2), 2180–2196,  
 624 doi:10.4319/lo.2008.53.5\_part\_2.2180.
- 625 Glenn, S. M., T. N. Miles, G. N. Seroka, Y. Xu, R. K. Forney, F. Yu, H. Roarty, O.  
 626 Schofield, and J. Kohut (2016), Stratified Coastal Ocean Interactions with Tropical  
 627 Cyclones, *Nat. Commun.*, *7*(08 March 2016), doi:10.1038/ncomms10887.
- 628 Haidvogel, D. B. et al. (2008), Ocean forecasting in terrain-following coordinates:  
 629 Formulation and skill assessment of the Regional Ocean Modeling System, *J.*  
 630 *Comput. Phys.*, *227*(7), 3595–3624, doi:10.1016/j.jcp.2007.06.016.
- 631 Hansen, J. et al. (2016), Ice melt, sea level rise and superstorms: evidence from  
 632 paleoclimate data, climate modeling, and modern observations that 2°C global  
 633 warming could be dangerous, *Atmos. Chem. Phys.*, *16*(6), 3761–3812,  
 634 doi:10.5194/acp-16-3761-2016.
- 635 Houghton, R. W., R. Schlitz, R. C. Beardsley, B. Butman, and J. L. Chamberlin (1982),  
 636 The Middle Atlantic Bight Cold Pool: Evolution of the Temperature Structure  
 637 During Summer 1979, *J. Phys. Oceanogr.*, *12*(10), 1019–1029, doi:10.1175/1520-  
 638 0485.
- 639 Jaimes, B., and L. K. Shay (2015), Enhanced Wind-Driven Downwelling Flow in Warm  
 640 Oceanic Eddy Features during the Intensification of Tropical Cyclone Isaac (2012):  
 641 Observations and Theory, *J. Phys. Oceanogr.*, *45*(6), 1667–1689, doi:10.1175/JPO-  
 642 D-14-0176.1.
- 643 Keen, T. R., and S. M. Glenn (1995), A coupled hydrodynamic-bottom boundary layer  
 644 model of storm and tidal flow in the Middle Atlantic Bight of North America, *J.*  
 645 *Phys. Oceanogr.*, *25*(3), 391–406.
- 646 Kim, H. S., C. Lozano, V. Tallapragada, D. Iredell, D. Sheinin, H. L. Tolman, V. M.  
 647 Gerald, and J. Sims (2014), Performance of ocean simulations in the coupled  
 648 HWRF-HYCOM model, *J. Atmos. Ocean. Technol.*, *31*(2), 545–559,  
 649 doi:10.1175/JTECH-D-13-00013.1.
- 650 Kossin, J. P., K. Emanuel, and G. Vecchi (2014), The poleward migration of the location

651 of tropical cyclone maximum intensity., *Nature*, 509(7500), 349–52,  
652 doi:10.1038/nature13278.

653 Lin, I.-I., C.-H. Chen, I.-F. Pun, W. T. Liu, and C.-C. Wu (2009), Warm ocean anomaly,  
654 air sea fluxes, and the rapid intensification of tropical cyclone Nargis (2008),  
655 *Geophys. Res. Lett.*, 36(3), 1–5, doi:10.1029/2008GL035815.

656 Miles, T., S. Glenn, and O. Schofield (2013), Temporal and spatial variability in fall  
657 storm induced sediment resuspension on the Mid-Atlantic Bight, *Cont. Shelf Res.*,  
658 63.

659 Miles, T. N., G. N. Seroka, J. T. Kohut, O. Schofield, and S. M. Glenn (2015), Glider  
660 observations and modeling of sediment transport in Hurricane Sandy, *J. Geophys.*  
661 *Res. Ocean.*, 120, 1771–1791, doi:10.1002/2014JC010474. Received.

662 NOAA National Centers for Environmental Prediction (2016), U.S. Coastal Relief  
663 Model, Available from: <http://www.ngdc.noaa.gov/mgg/coastal/crm.html>

664 Peduzzi, P., B. Chatenoux, H. Dao, A. De Bono, C. Herold, J. Kossin, F. Mouton, and O.  
665 Nordbeck (2012), Global trends in tropical cyclone risk, *Nat. Clim. Chang.*, 2(4),  
666 289–294, doi:10.1038/nclimate1410.

667 Price, J. F. (1981), Upper Ocean Response to a Hurricane, *J. Phys. Oceanogr.*, 11(2),  
668 153–175, doi:10.1175/1520-0485(1981)011<0153:UORTAH>2.0.CO;2.

669 Roarty, H. et al. (2010), Operation and Application of a Regional High-Frequency Radar  
670 Network in the Mid-Atlantic Bight, *Mar. Technol. Soc. J.*, 44(6), 133–145,  
671 doi:10.4031/MTSJ.44.6.5.

672 Ruiz, S., L. Renault, B. Garau, and J. Tintoré (2012), Underwater glider observations and  
673 modeling of an abrupt mixing event in the upper ocean, *Geophys. Res. Lett.*, 39(1),  
674 n/a–n/a, doi:10.1029/2011GL050078.

675 Schofield, O. et al. (2007), Slocum Gliders: Robust and ready, *J. F. Robot.*, 24(6), 473–  
676 485, doi:10.1002/rob.20200.

677 Schofield, O., R. J. Chant, B. Cahill, and R. Castelao (2008), The Decadal View of the  
678 Mid-Atlantic Bight from the COOLroom: Is Our Coastal System Changing?,  
679 *Oceanography*, 21(4), 108–117.

680 Seroka, G. N., T. N. Miles, Y. Xu, J. T. Kohut, O. Schofield, and S. M. Glenn (2016),  
681 Hurricane Irene Sensitivity to Stratified Coastal Ocean Cooling, *Mon. Weather Rev.*,  
682 144(9), 3507–3530, doi:10.1175/MWR-D-15-0452.1.

683 Sherman, J., R. E. Davis, W. B. Owens, and J. Valdes (2001), The Autonomous  
684 Underwater Glider “Spray,” *IEEE J. Ocean. Eng.*, 26(4), 437–446.

685 Sopko, S. P., and R. J. Falvey (2014), *Annual Tropical Cyclone Report 2014: Joint*  
686 *Typhoon Warning Center*.

687 Tallapragada, V., C. Kieu, Y. Kwon, S. Trahan, Q. Liu, Z. Zhang, and I.-H. Kwon  
688 (2014), Evaluation of Storm Structure from the Operational HWRF during 2012  
689 Implementation, *Mon. Weather Rev.*, 142(11), 4308–4325, doi:10.1175/MWR-D-  
690 13-00010.1.

691 Umlauf, L., and H. Burchard (2003), A generic length-scale equation for geophysical  
692 turbulence models, *J. Mar. Res.*, 61(2), 235–265,  
693 doi:10.1357/002224003322005087.

694 Warner, J. C., C. R. Sherwood, H. G. Arango, and R. P. Signell (2005), Performance of  
695 four turbulence closure models implemented using a generic length scale method,  
696 *Ocean Model.*, 8(1-2), 81–113, doi:10.1016/j.ocemod.2003.12.003.

697 Wilkin, J. L., and E. J. Hunter (2013), An assessment of the skill of real-time models of  
698 Mid-Atlantic Bight continental shelf circulation, *J. Geophys. Res. Ocean.*, *118*(6),  
699 2919–2933, doi:10.1002/jgrc.20223.  
700 Zhang, W. G., and G. G. Gawarkiewicz (2015), Dynamics of the direct intrusion of Gulf  
701 Stream ring water onto the Mid-Atlantic Bight shelf, *Geophys. Res. Lett.*, *42*(18),  
702 7687–7695, doi:10.1002/2015GL065530.  
703

704 **Figure Captions**

705

706 **Figure 1. Irene and Barry.** HF radar surface ocean current 1-hour center-averaged maps  
707 for Irene and Barry before eye passage by RU16 (Irene, top left) and RU17 (Barry, top  
708 right). National Hurricane Center (NHC) best track in black, with large black arrow  
709 indicating general direction of surface currents. Location of RU16 and RU17 shown with  
710 red triangles. Time series at glider locations of temperature with thermocline depth in  
711 black contour, transition layer depth (see Glenn et al. [2016] for definitions) in magenta  
712 contour, and large white arrows indicating general direction of layer currents (second row  
713 from top); cross-shelf currents (third row from top); along-shelf currents (fourth row);  
714 and surface to bottom shear for Barry (bottom right). Currents and shear are smoothed  
715 using the MATLAB “smooth” function using a span of 8.

716

717 **Figure 2. Irene.** AVHRR Multi-Channel SST (MCSST) (top left) and ROMS ESPreSSO  
718 re-run SST (top right) pre-storm for Irene; the same for post-storm in middle panels, and  
719 for post-storm minus pre-storm in bottom panels. Dashed magenta contour is 50m  
720 isobath, and solid magenta contour is 200m isobath. RU16 location throughout the storm  
721 period plotted as yellow triangle, NHC best track for Irene in black with red outlined  
722 dots, small black dots in line northwest to southeast indicating cross section location  
723 taken for Hövmoller figures below, and large red dots along this black line indicating  
724 profile locations taken for temperature diagnostic Fig. 14 below.

725

726 **Figure 3. Irene.** RU16 glider temperature ( $^{\circ}\text{C}$ ) (left) and ROMS ESPreSSO re-run  
727 temperature ( $^{\circ}\text{C}$ ) (right) at the closest ESPreSSO grid point to the average RU16 glider  
728 location during the storm.

729

730 **Figure 4. Barry.** The same as Fig. 2, but for Barry. NDBC station ALSN6 and RU17  
731 glider locations indicated with yellow triangles. Northern cross section location used for  
732 Barry plotted as west-northwest to east-southeast black dots just north of the Hudson  
733 Canyon, and large red dots along this black line indicating profile locations taken for  
734 temperature diagnostic Fig. 15 below. A third panel on bottom (bottom right) is added for  
735 Barry with post-storm minus pre-storm time difference chosen to maximize the cooling  
736 across the map in the ROMS ESPreSSO re-run.

737

738 **Figure 5. Barry.** The same as Fig. 3, but for RU17 glider in Barry. RU17 only sampled  
739 to  $\sim 60\text{m}$  even though full water column depth was  $>80\text{m}$ .

740

741 **Figure 6. Irene.** Hövmollers of ROMS ESPreSSO re-run SST ( $^{\circ}\text{C}$ , top left), surface  
742 cross-shelf currents ( $\text{m s}^{-1}$ , top middle), and surface along-shelf currents ( $\text{m s}^{-1}$ , top right),  
743 with positive reds offshore/northeastward and negative blues onshore/southwestward for  
744 cross-shelf/along-shelf currents. Bottom row the same as top row but for the bottom of  
745 the water column. Eye passage in NAM atmospheric forcing marked with the horizontal  
746 dashed line, and RU16 glider location marked with the vertical dashed line. Vertical solid  
747 lines in left panels labeled 1 (upwelling), 2 (near RU16), 3 (in Cold Pool core), and 4 (in

748 deep water) are locations where temperature diagnostics are performed in Fig. 14. Water  
749 depth (m) along the cross section is plotted in the panels below the Hövmoller panels.

750

751 **Figure 7. Irene.** Same formatted Hövmoller as in Fig. 6, but for bulk surface to bottom  
752 cross- and along-shelf shear (left,  $\text{m s}^{-1}$ ). This bulk shear is calculated according to the  
753 equation in the header: square root of the sum of the squares of the surface to bottom  
754 cross- and along-shelf shears. Right panel is the same as left but for 0 substituted for  
755 bottom currents.

756

757 **Figure 8. Irene.** Hövmollers of the cross-shelf depth-averaged momentum balance terms  
758 ( $\text{m s}^{-2}$ ), with positive reds offshore and negative blues onshore. Horizontal diffusion was  
759 small and thus not plotted.

760

761 **Figure 9. Irene.** Same as Fig. 8 but for along-shelf depth-averaged momentum balance  
762 terms ( $\text{m s}^{-2}$ ), with positive reds northeastward and negative blues southwestward.

763

764 **Figure 10. Barry.** Same as Fig. 6 but for Barry, with ALSN6 and RU17 locations plotted  
765 as vertical dashed lines. Vertical solid lines in left panels labeled 2 (near ALSN6), 2 (in  
766 warm strip), 3 (in Cold Pool core), 4 (near RU17), and 5 (in deep water) are locations  
767 where temperature diagnostics are performed in Fig. 15.

768

769 **Figure 11. Barry.** Same as Fig. 7 (bulk surface to bottom shear analysis), but for Barry.

770

771 **Figure 12. Barry.** Same as Fig. 8 (Hövmoller cross-shelf depth-averaged momentum  
772 balance terms), but for Barry.

773

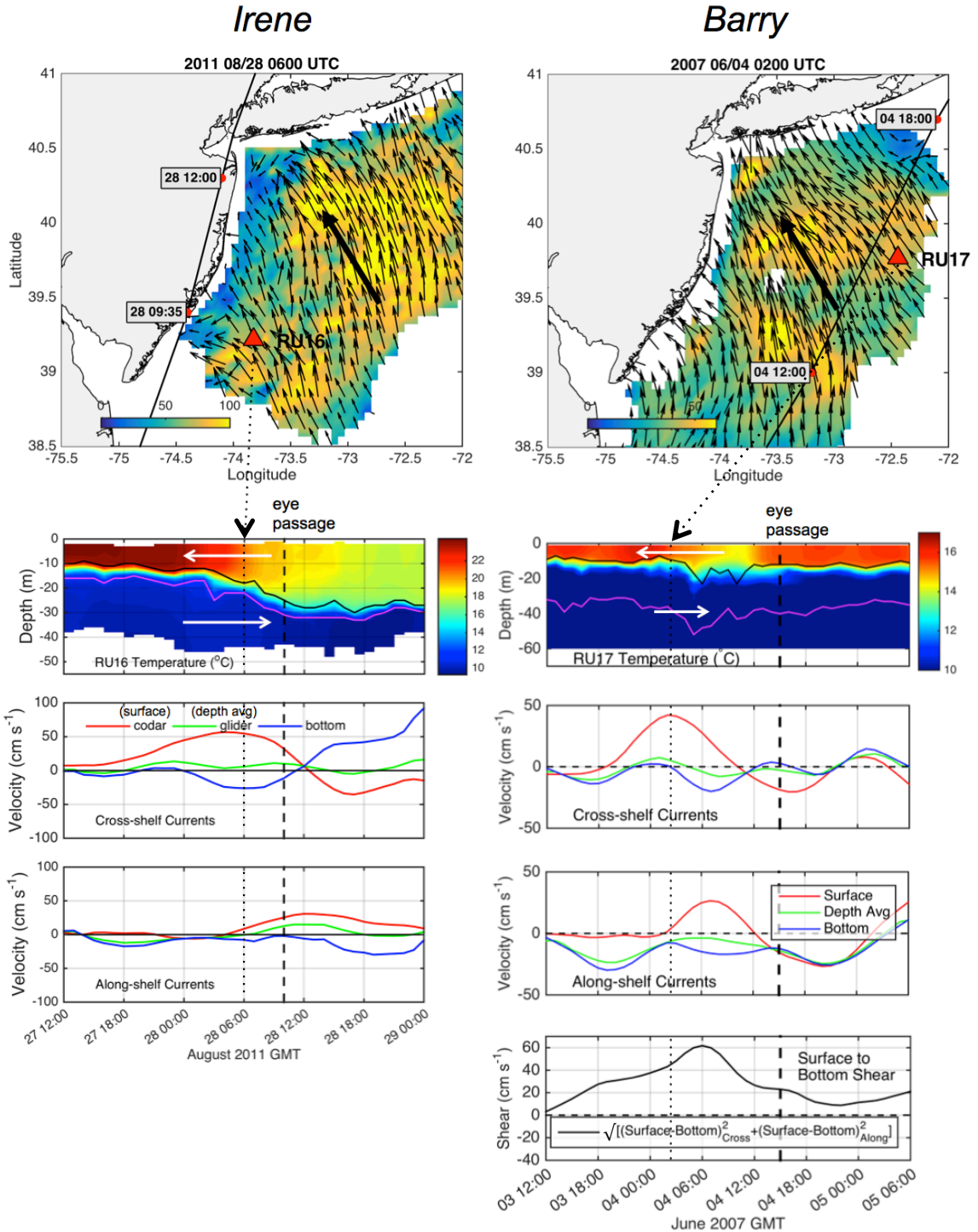
774 **Figure 13. Barry.** Same as Fig. 9 (Hövmoller along-shelf depth-averaged momentum  
775 balance terms), but for Barry.

776

777 **Figure 14. Irene.** Temperature diagnostic equation terms at points 1-4 marked in Fig. 2's  
778 red dots ordered 1-4 northwest to southeast, and in Fig. 6's left panels, with full  
779 temperature rate term at top, vertical diffusion in middle, and vertical + horizontal  
780 advection at bottom ( $^{\circ}\text{C s}^{-1}$ ). Horizontal diffusion is small and thus not plotted. Eye  
781 passage marked with vertical dashed line. At point 4, only the top 500m of the water  
782 column is plotted.

783

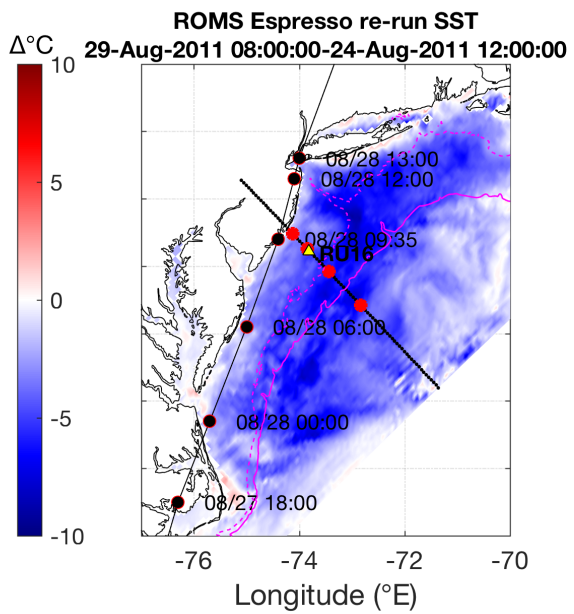
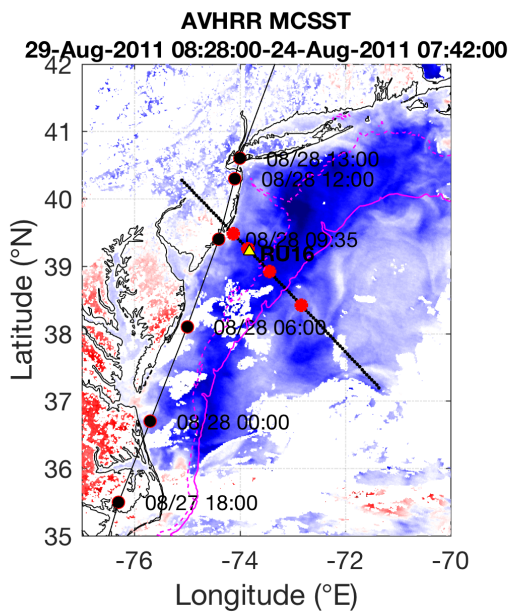
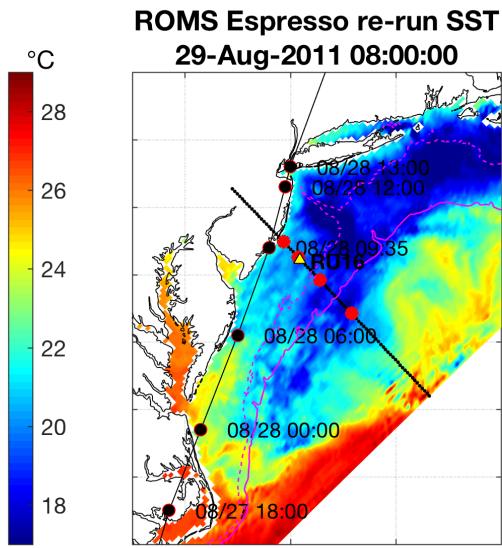
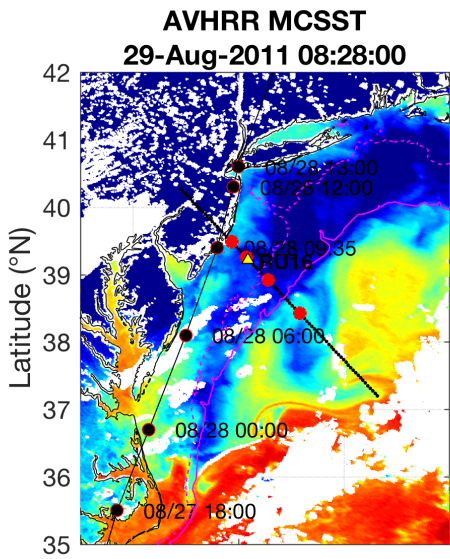
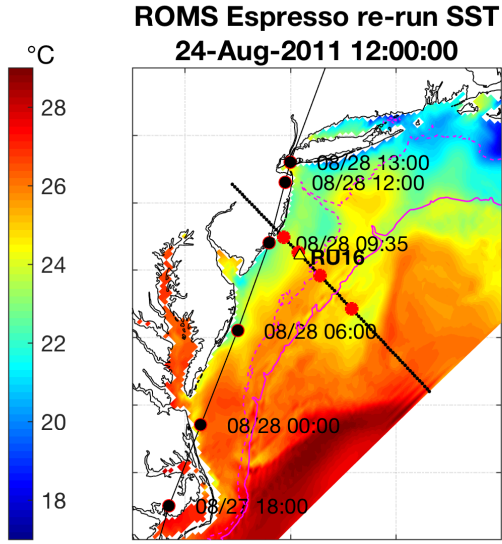
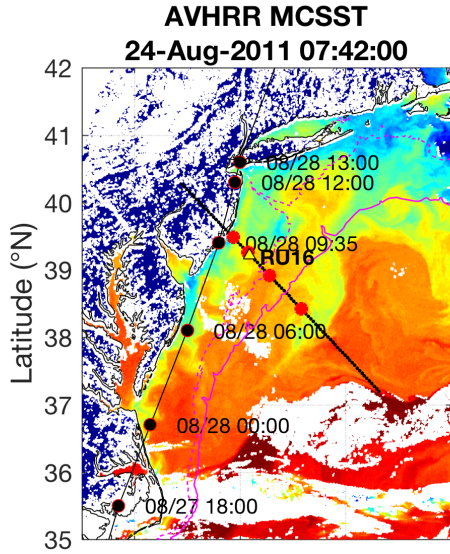
784 **Figure 15. Barry.** Same as Fig. 14 (temperature diagnostic equation terms) but for Barry.  
785 Points 1-5 are marked in Fig. 4's red dots ordered 1-5 west-northwest to east-southeast,  
786 and in Fig. 10's left panels.



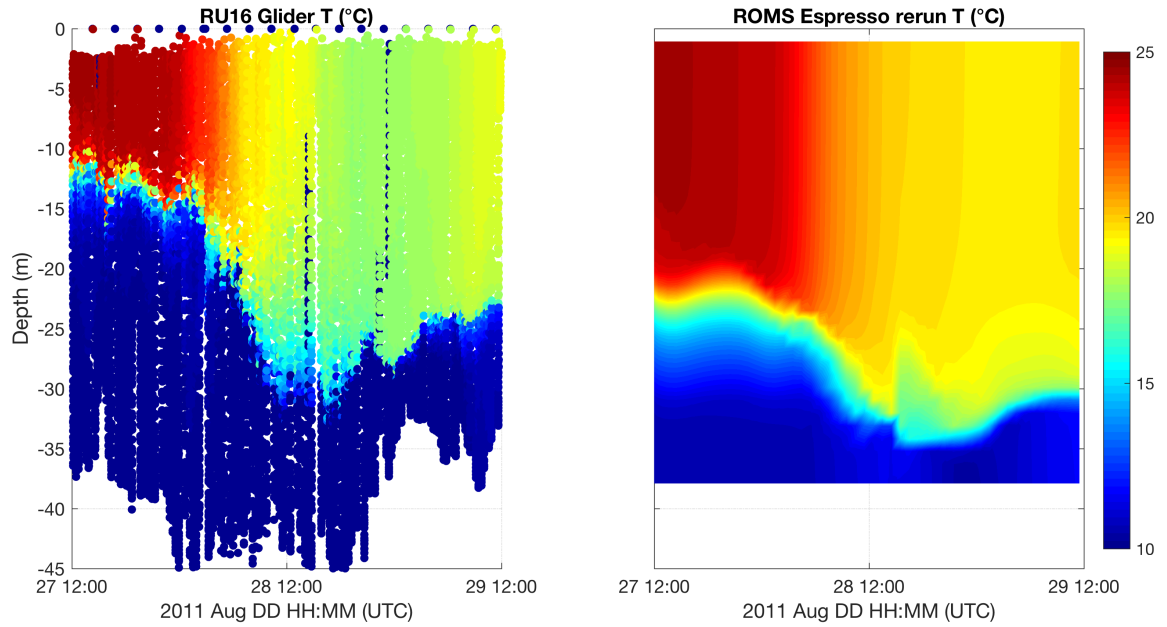
787  
788  
789  
790  
791  
792  
793  
794

**Figure 1. Irene and Barry.** HF radar surface ocean current 1-hour center-averaged maps for Irene and Barry before eye passage by RU16 (Irene, top left) and RU17 (Barry, top right). National Hurricane Center (NHC) best track in black, with large black arrow indicating general direction of surface currents. Location of RU16 and RU17 shown with red triangles. Time series at glider locations of temperature with thermocline depth in black contour, transition layer depth (see Glenn et al. [2016] for definitions) in magenta contour, and large white arrows indicating general direction of layer currents (second row

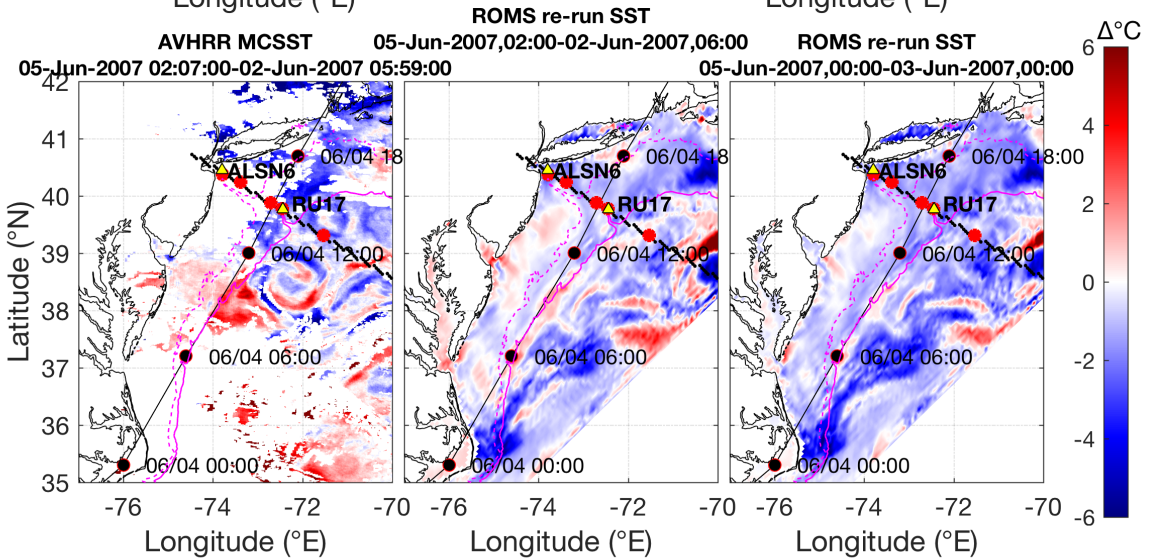
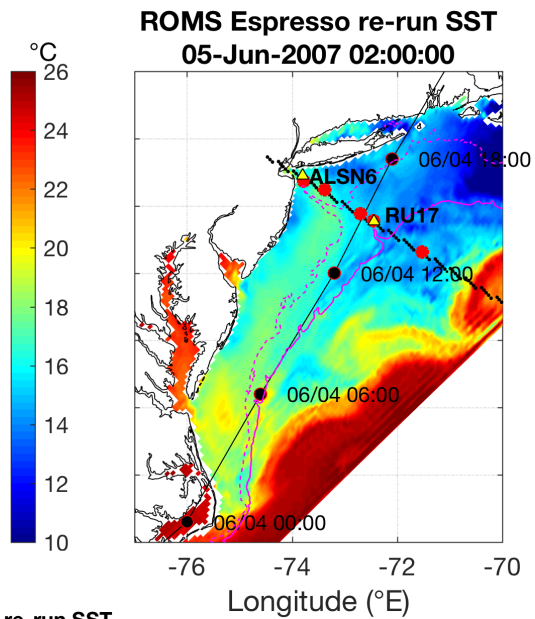
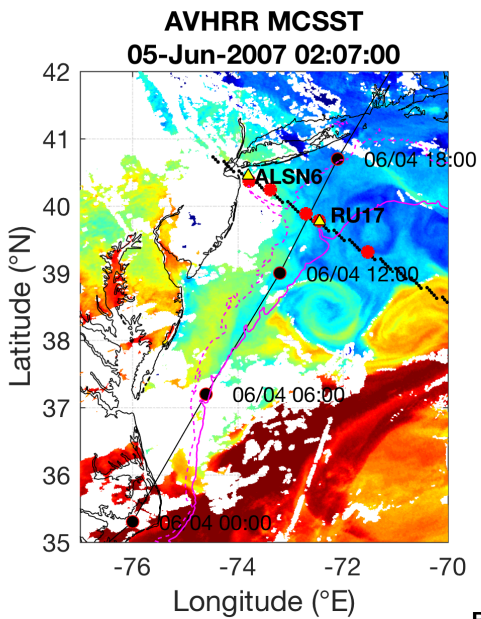
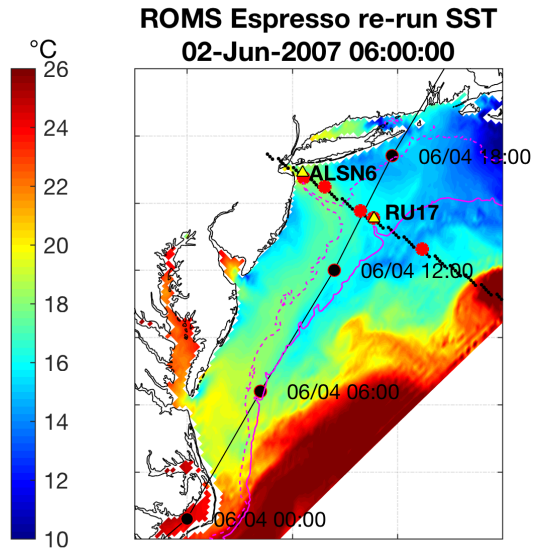
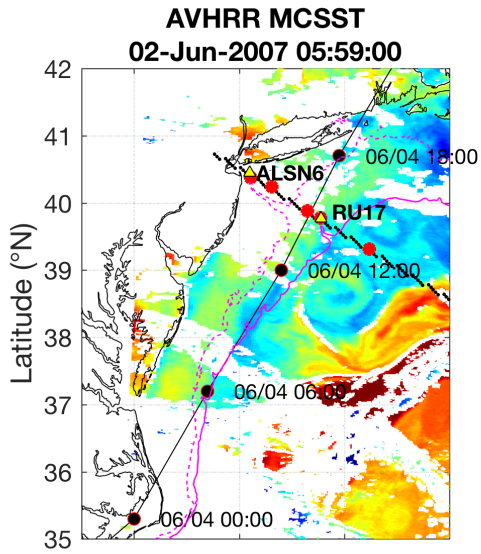
795 from top); cross-shelf currents (third row from top); along-shelf currents (fourth row);  
796 and surface to bottom shear for Barry (bottom right). Currents and shear are smoothed  
797 using the MATLAB “smooth” function using a span of 8.  
798  
799



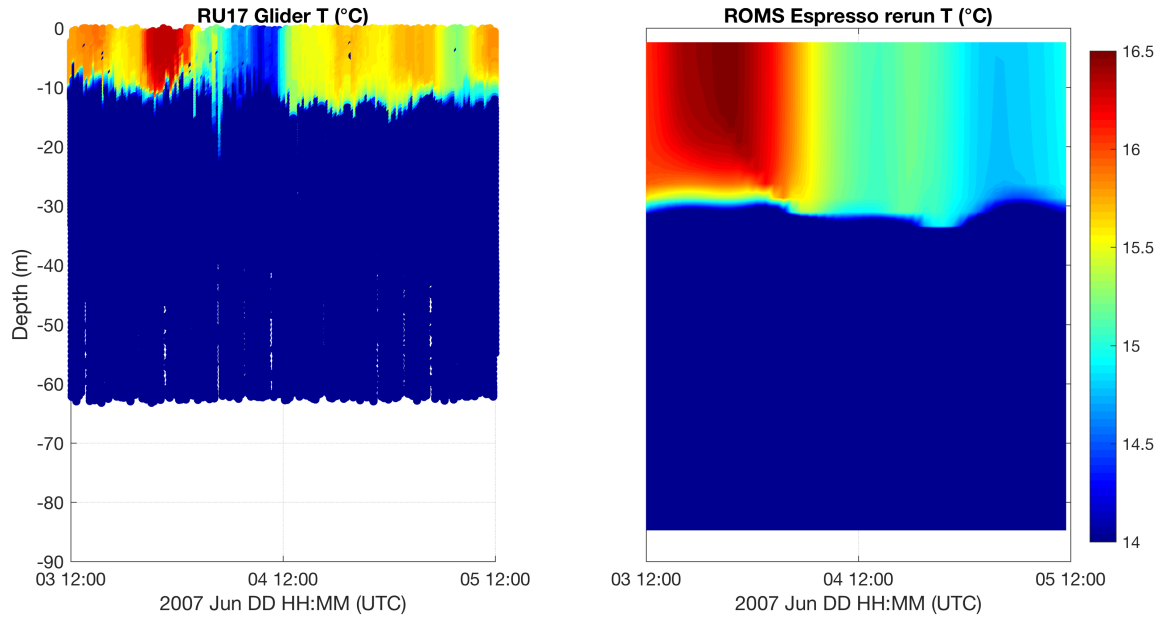
801 **Figure 2. Irene.** AVHRR Multi-Channel SST (MCSST) (top left) and ROMS EPreSSO  
802 re-run SST (top right) pre-storm for Irene; the same for post-storm in middle panels, and  
803 for post-storm minus pre-storm in bottom panels. Dashed magenta contour is 50m  
804 isobath, and solid magenta contour is 200m isobath. RU16 location throughout the storm  
805 period plotted as yellow triangle, NHC best track for Irene in black with red outlined  
806 dots, small black dots in line northwest to southeast indicating cross section location  
807 taken for Hövmoller figures below, and large red dots along this black line indicating  
808 profile locations taken for temperature diagnostic Fig. 14 below.  
809  
810  
811  
812



813  
 814 **Figure 3. Irene.** RU16 glider temperature (°C) (left) and ROMS ESPreSSO re-run  
 815 temperature (°C) (right) at the closest ESPreSSO grid point to the average RU16 glider  
 816 location during the storm.  
 817  
 818

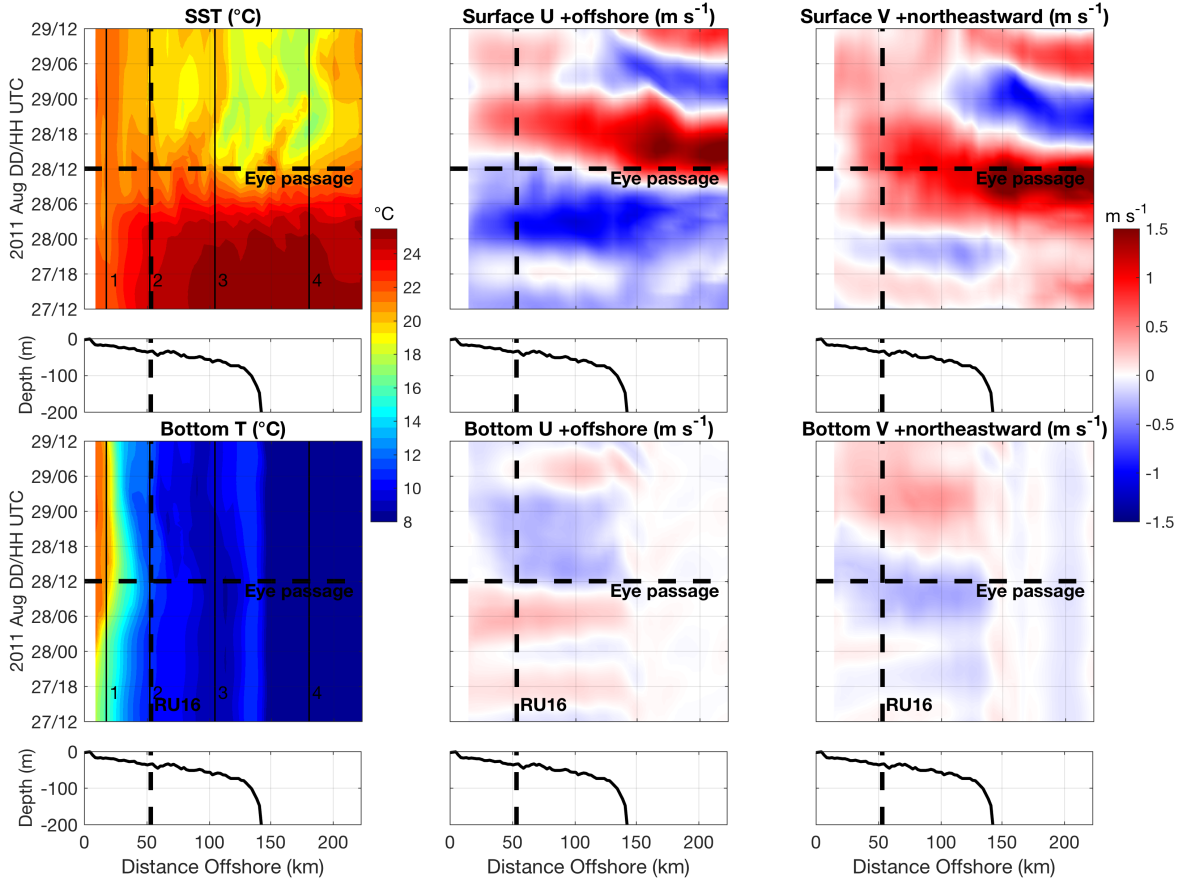


820 **Figure 4. Barry.** The same as Fig. 2, but for Barry. NDBC station ALSN6 and RU17  
821 glider locations indicated with yellow triangles. Northern cross section location used for  
822 Barry plotted as west-northwest to east-southeast black dots just north of the Hudson  
823 Canyon, and large red dots along this black line indicating profile locations taken for  
824 temperature diagnostic Fig. 15 below. A third panel on bottom (bottom right) is added for  
825 Barry with post-storm minus pre-storm time difference chosen to maximize the cooling  
826 across the map in the ROMS ESPreSSO re-run.  
827  
828



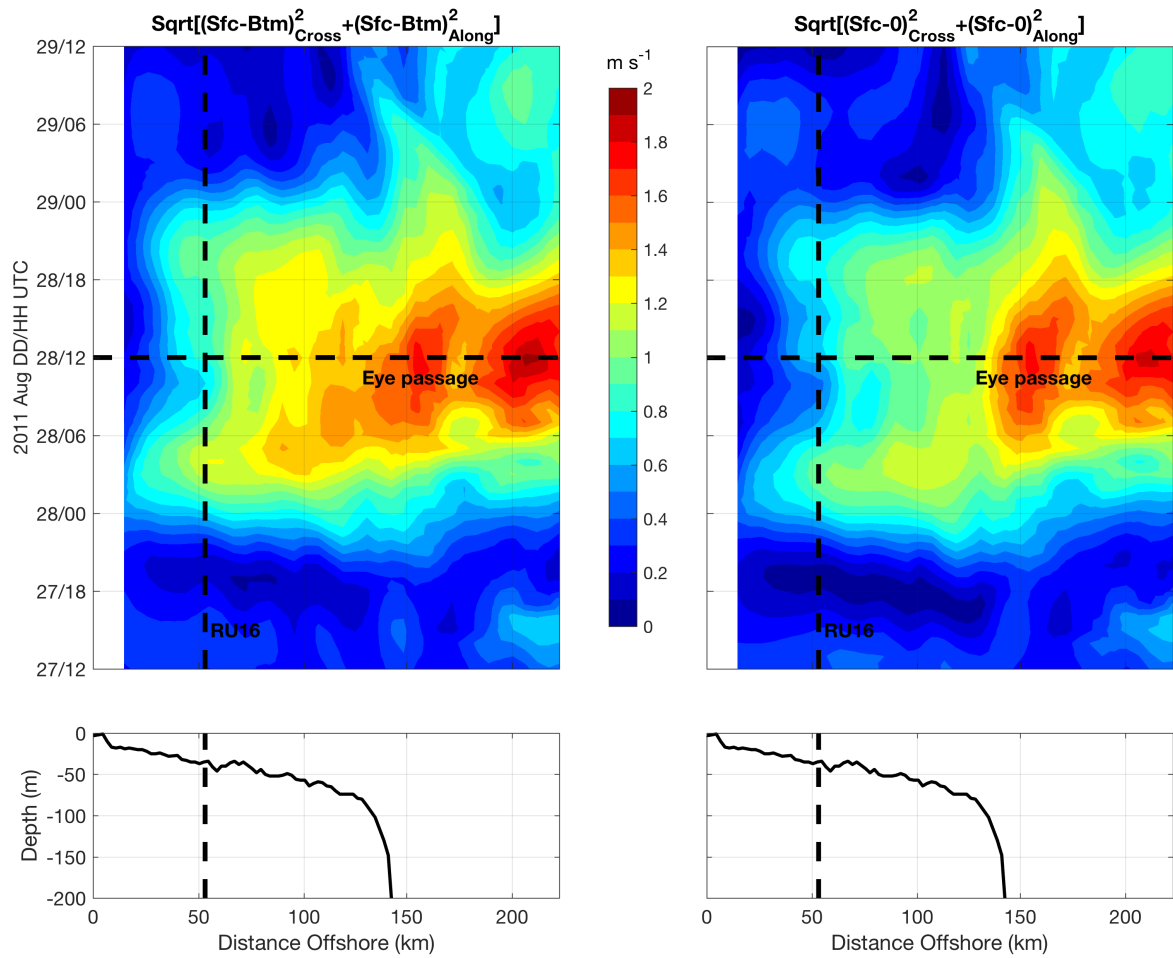
829  
 830  
 831  
 832  
 833  
 834

**Figure 5. Barry.** The same as Fig. 3, but for RU17 glider in Barry. RU17 only sampled to ~60m even though full water column depth was >80m.



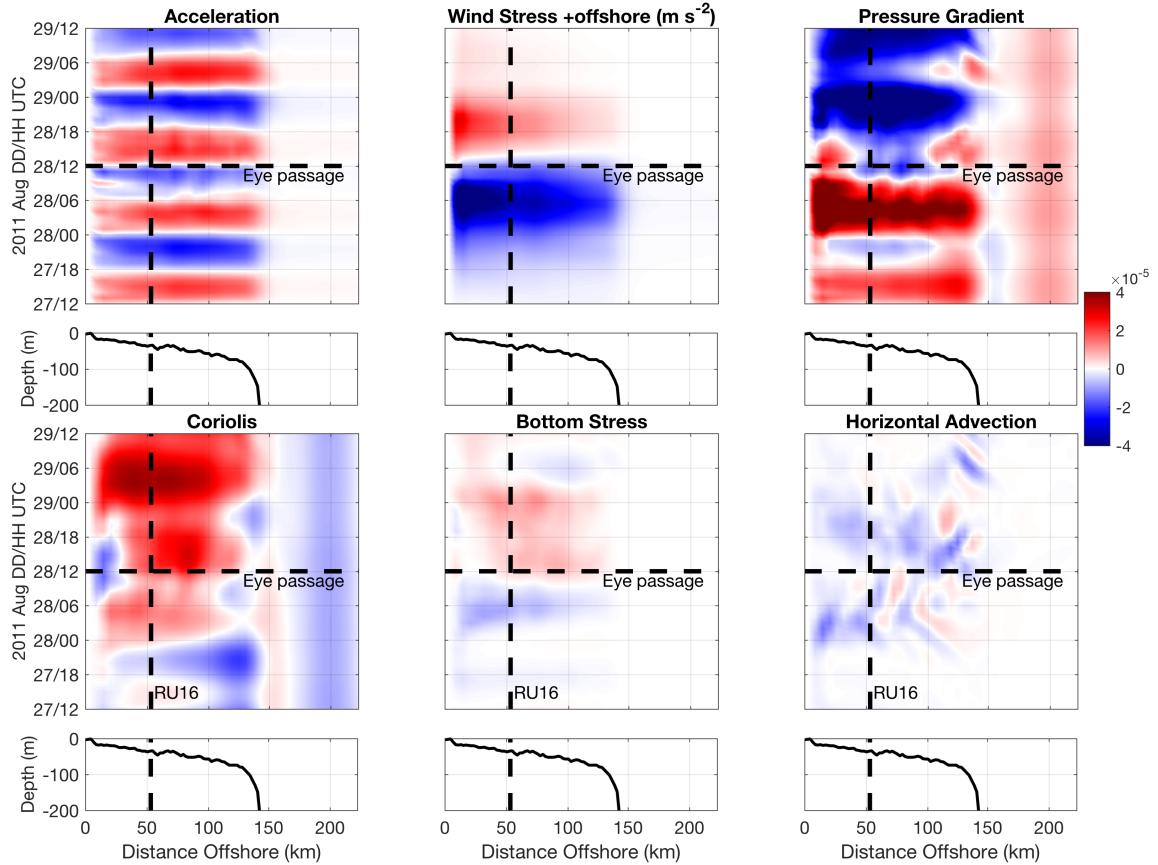
835  
836  
837  
838  
839  
840  
841  
842  
843  
844  
845  
846

**Figure 6. Irene.** Hövmollers of ROMS ESPreSSO re-run SST ( $^{\circ}\text{C}$ , top left), surface cross-shelf currents ( $\text{m s}^{-1}$ , top middle), and surface along-shelf currents ( $\text{m s}^{-1}$ , top right), with positive reds offshore/northeastward and negative blues onshore/southwestward for cross-shelf/along-shelf currents. Bottom row the same as top row but for the bottom of the water column. Eye passage in NAM atmospheric forcing marked with the horizontal dashed line, and RU16 glider location marked with the vertical dashed line. Vertical solid lines in left panels labeled 1 (upwelling), 2 (near RU16), 3 (in Cold Pool core), and 4 (in deep water) are locations where temperature diagnostics are performed in Fig. 14. Water depth (m) along the cross section is plotted in the panels below the Hövmoller panels.



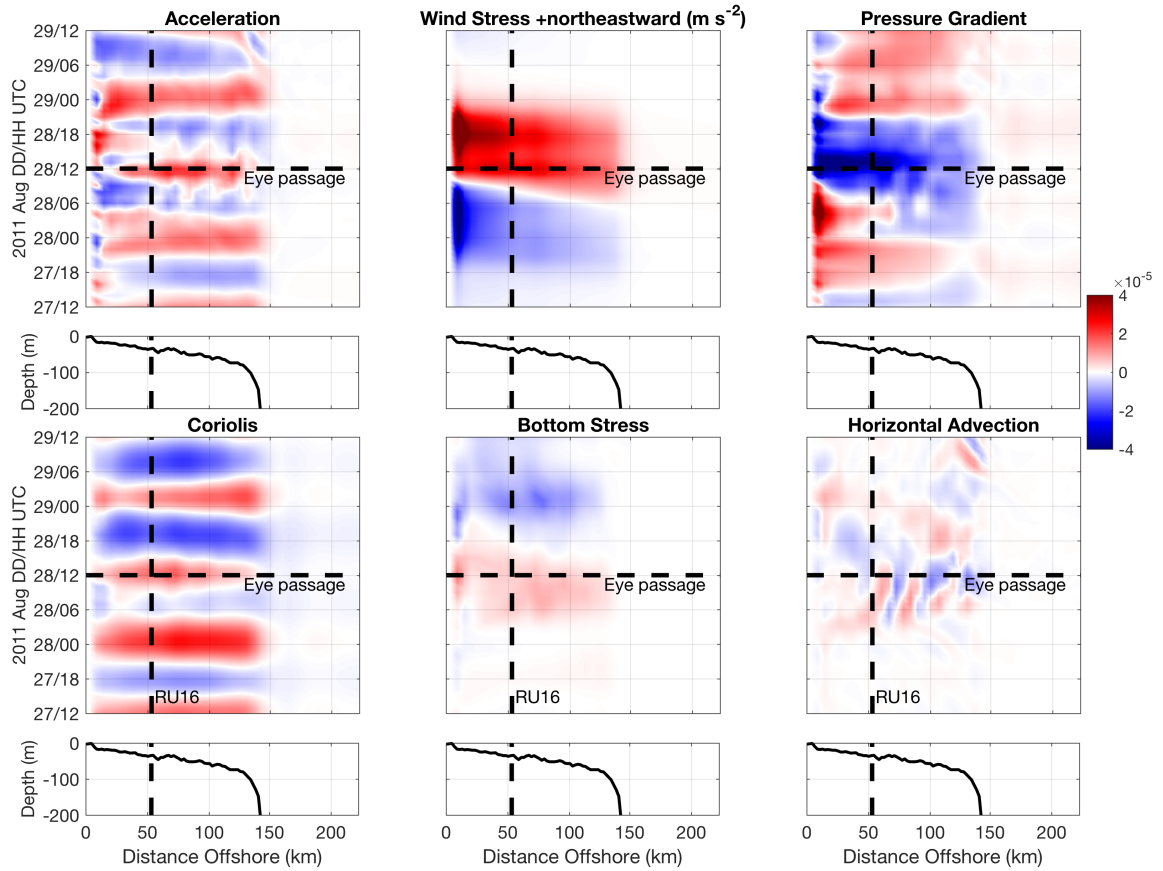
847  
848  
849  
850  
851  
852  
853  
854

**Figure 7. Irene.** Same formatted Hövmoller as in Fig. 6, but for bulk surface to bottom cross- and along-shelf shear (left,  $\text{m s}^{-1}$ ). This bulk shear is calculated according to the equation in the header: square root of the sum of the squares of the surface to bottom cross- and along-shelf shears. Right panel is the same as left but for 0 substituted for bottom currents.

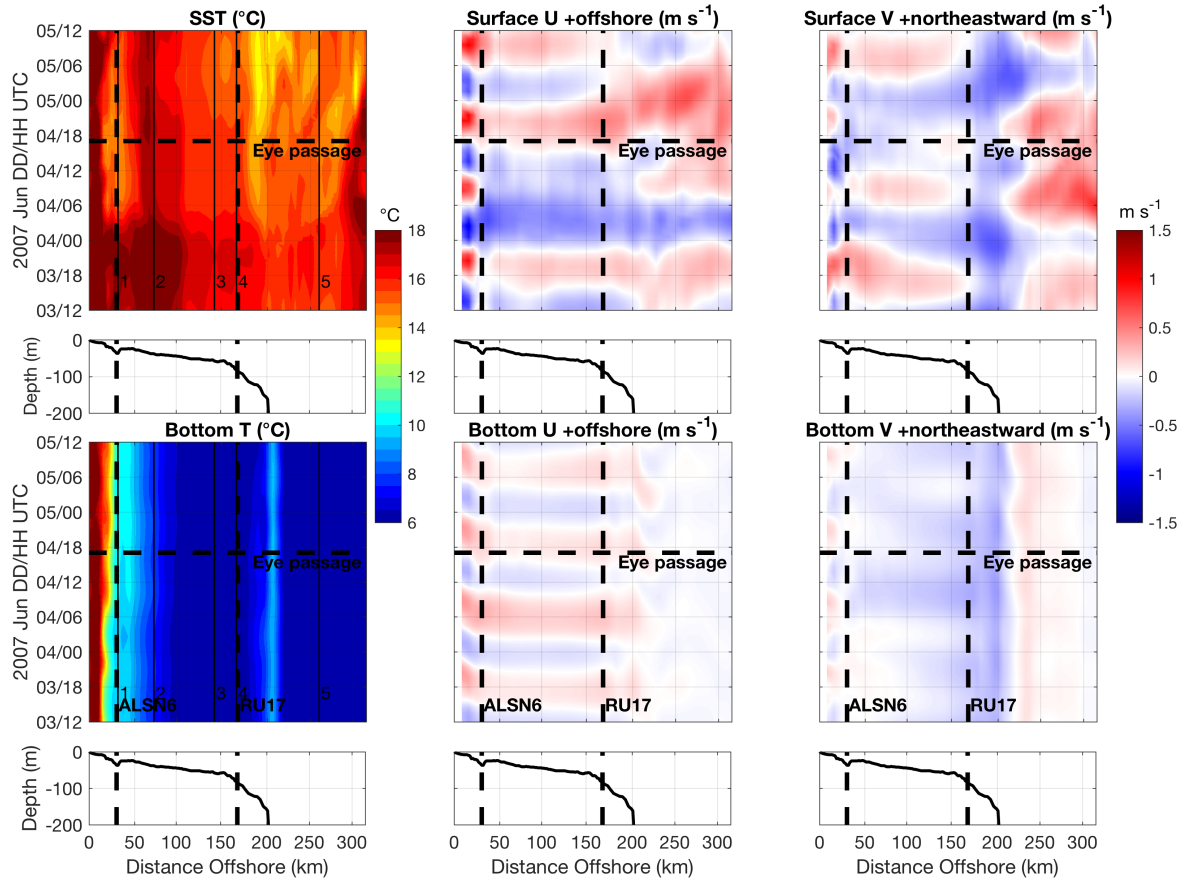


855  
 856  
 857  
 858  
 859  
 860  
 861

**Figure 8. Irene.** Hövmollers of the cross-shelf depth-averaged momentum balance terms ( $\text{m s}^{-2}$ ), with positive reds offshore and negative blues onshore. Horizontal diffusion was small and thus not plotted.

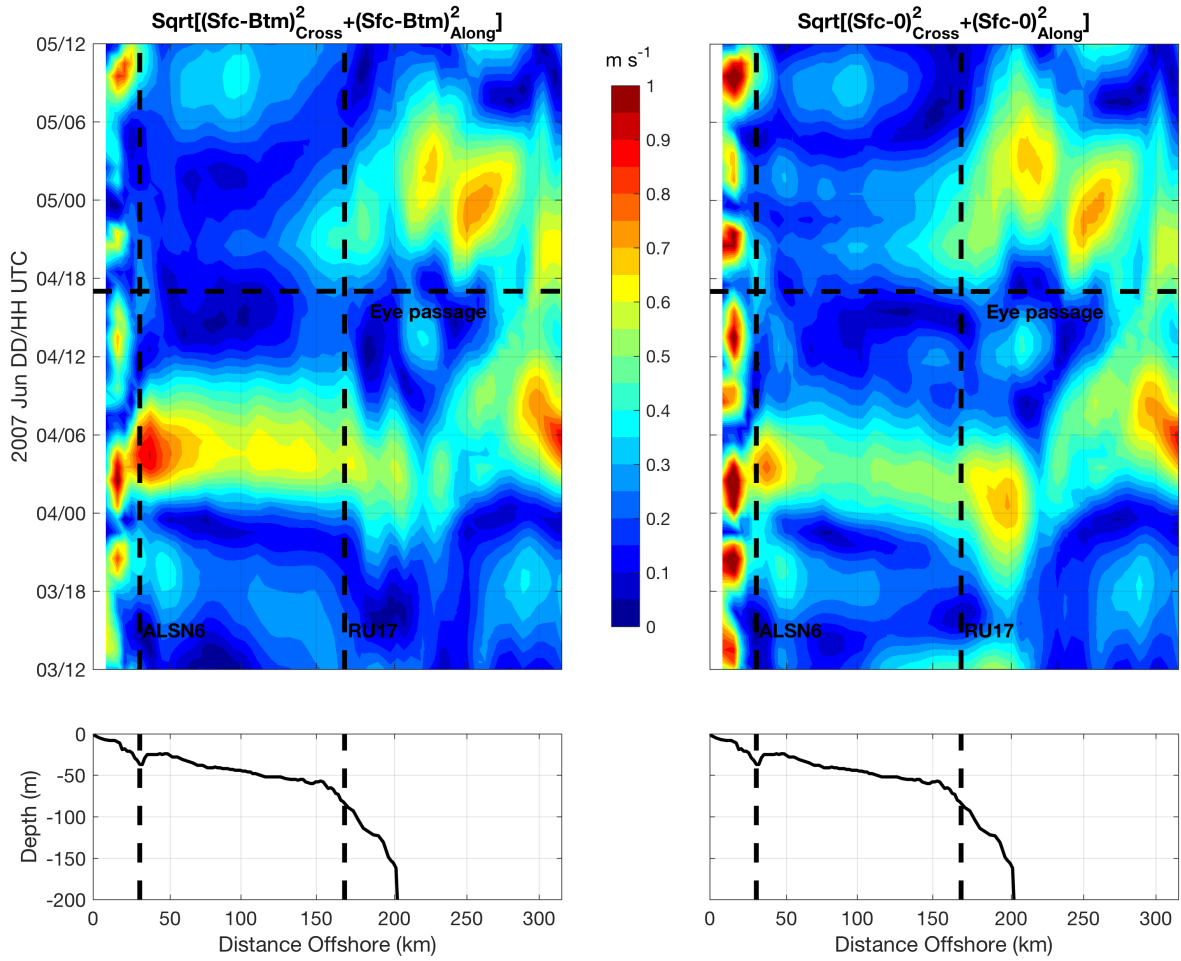


862  
 863 **Figure 9. Irene.** Same as Fig. 8 but for along-shelf depth-averaged momentum balance  
 864 terms (m s<sup>-2</sup>), with positive reds northeastward and negative blues southwestward.  
 865  
 866



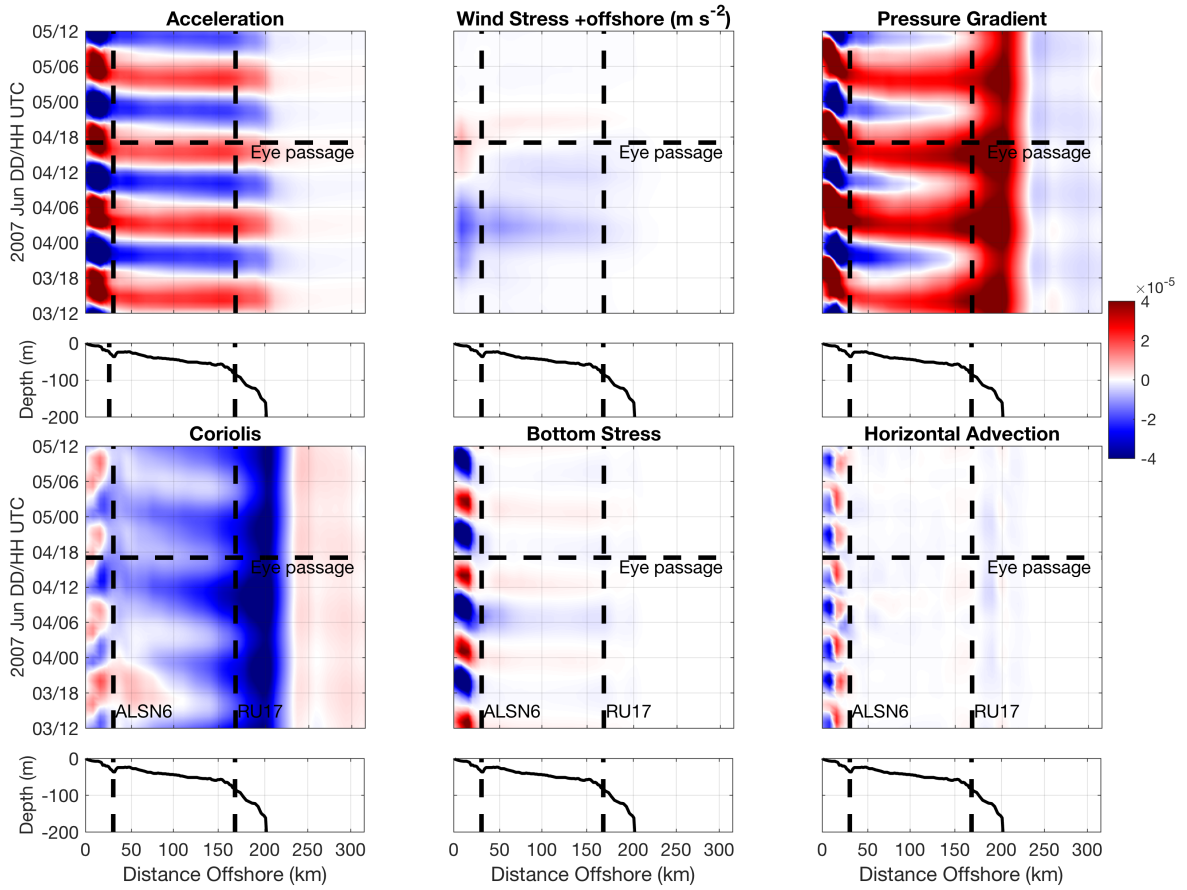
867  
 868  
 869  
 870  
 871  
 872  
 873

**Figure 10. Barry.** Same as Fig. 6 but for Barry, with ALSN6 and RU17 locations plotted as vertical dashed lines. Vertical solid lines in left panels labeled 2 (near ALSN6), 2 (in warm strip), 3 (in Cold Pool core), 4 (near RU17), and 5 (in deep water) are locations where temperature diagnostics are performed in Fig. 15.



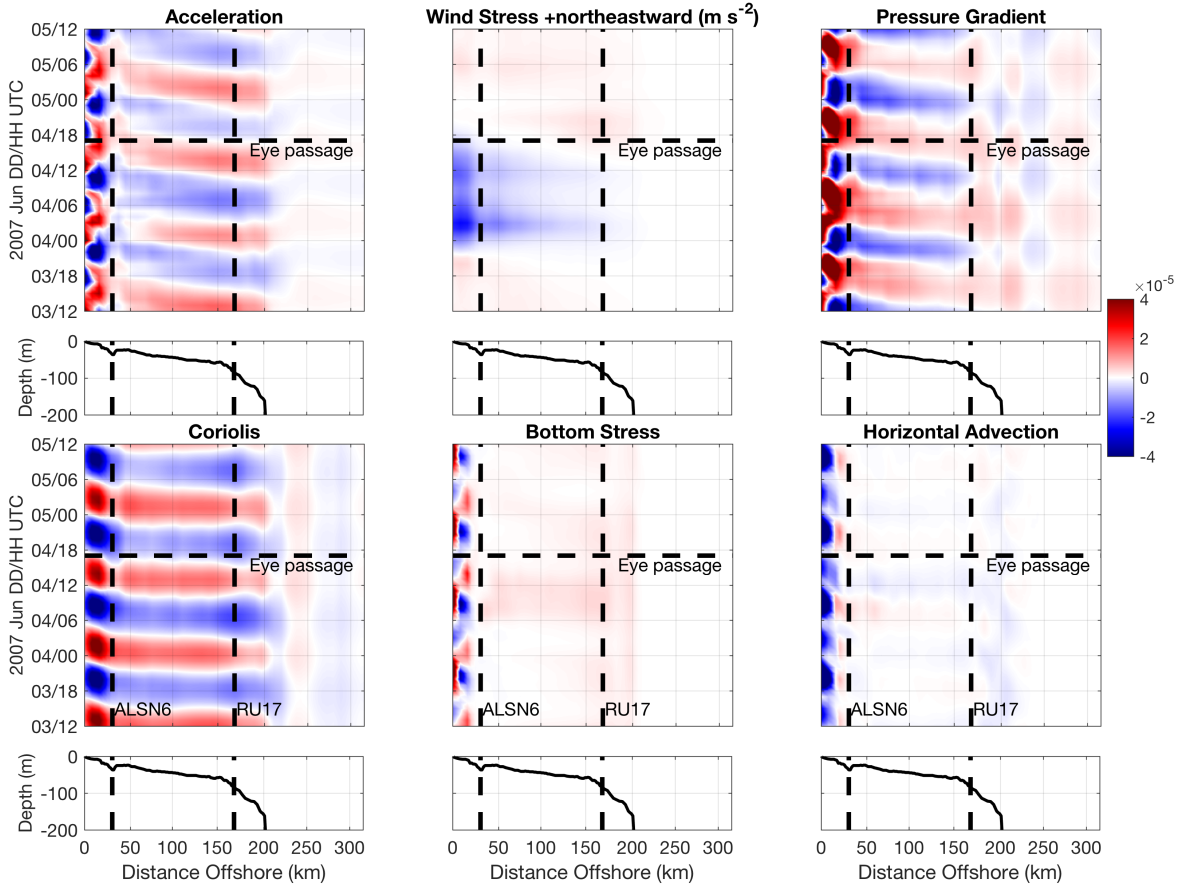
874  
875  
876  
877

**Figure 11. Barry.** Same as Fig. 7 (bulk surface to bottom shear analysis), but for Barry.



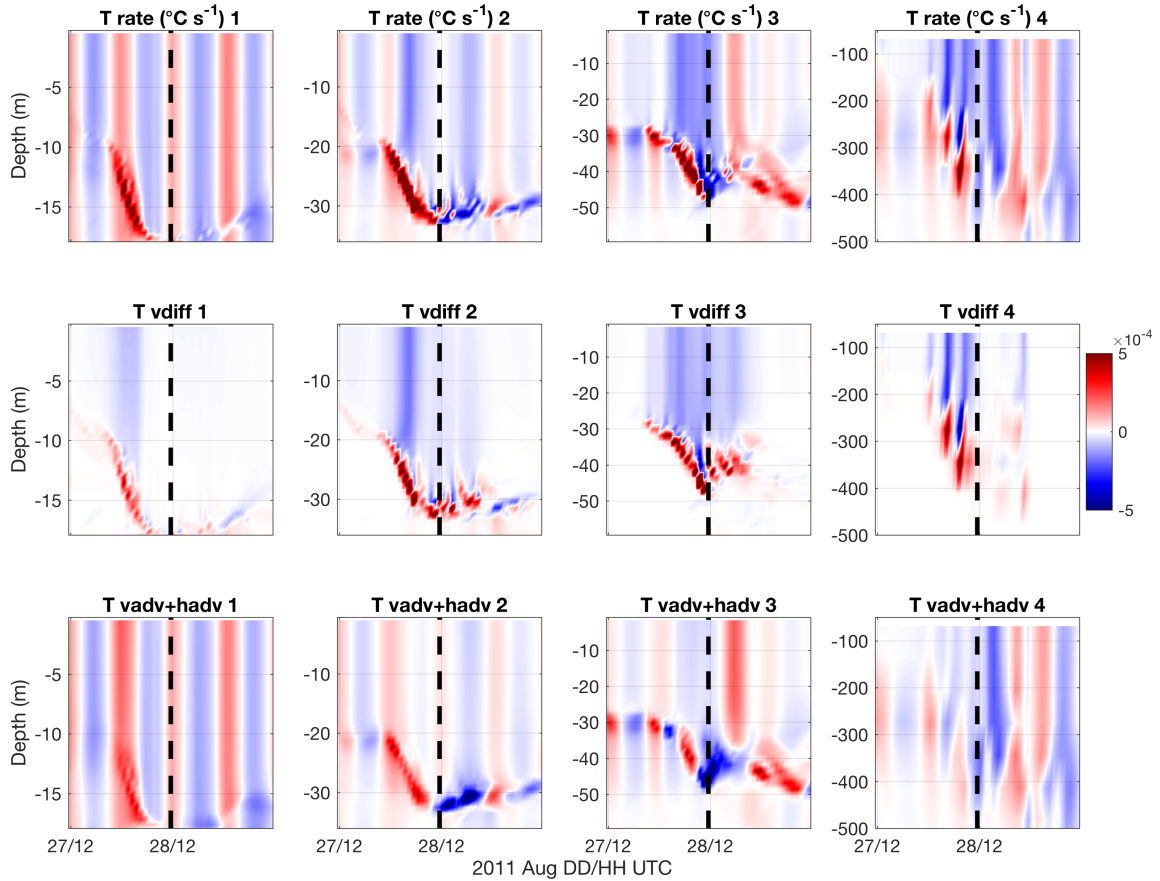
878  
 879  
 880  
 881  
 882

**Figure 12. Barry.** Same as Fig. 8 (Hövmoller cross-shelf depth-averaged momentum balance terms) but for Barry.



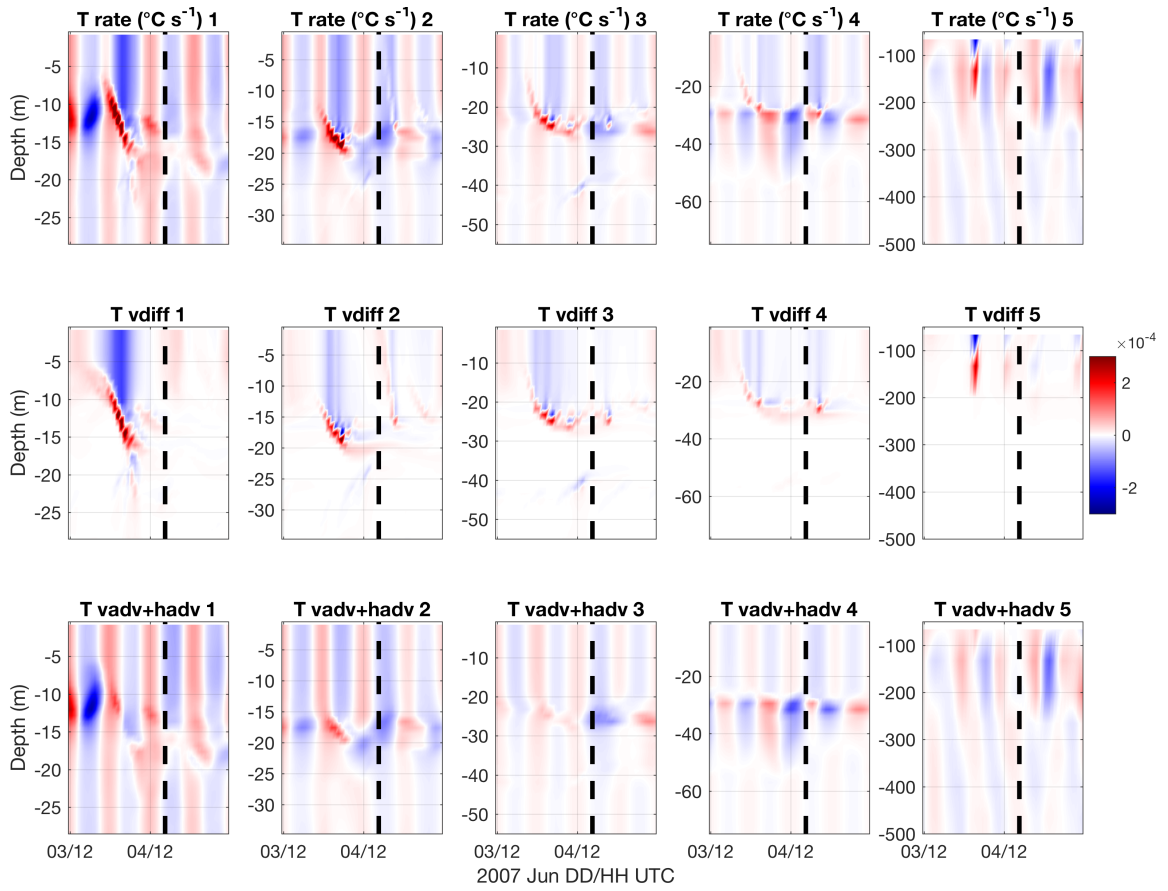
883  
 884  
 885  
 886  
 887

**Figure 13. Barry.** Same as Fig. 9 (Hövmoller along-shelf depth-averaged momentum balance terms) but for Barry.



888  
 889  
 890  
 891  
 892  
 893  
 894  
 895  
 896

**Figure 14. Irene.** Temperature diagnostic equation terms at points 1-4 marked in Fig. 2's red dots ordered 1-4 northwest to southeast, and in Fig. 6's left panels, with full temperature rate term at top, vertical diffusion in middle, and vertical + horizontal advection at bottom ( $^{\circ}\text{C s}^{-1}$ ). Horizontal diffusion is small and thus not plotted. Eye passage marked with vertical dashed line. At point 4, only the top 500m of the water column is plotted.



897  
 898  
 899  
 900

**Figure 15. Barry.** Same as Fig. 14 (temperature diagnostic equation terms) but for Barry. Points 1-5 are marked in Fig. 4's red dots ordered 1-5 west-northwest to east-southeast, and in Fig. 10's left panels.